

## Mechanics of stretchable inorganic electronic materials

J. Song<sup>a)</sup>

*Department of Mechanical and Aerospace Engineering, University of Miami, Coral Gables, Florida 33146*

H. Jiang

*Department of Mechanical and Aerospace Engineering, Arizona State University, Tempe, Arizona 85287*

Y. Huang

*Department of Civil and Environmental Engineering and Department of Mechanical Engineering, Northwestern University, Evanston, Illinois 60208*

J. A. Rogers<sup>a)</sup>

*Department of Materials Science and Engineering, Department of Mechanical Science and Engineering, Department of Electrical and Computer Engineering, Department of Chemistry, and Frederick Seitz Materials Research Laboratory, University of Illinois at Urbana-Champaign, Urbana, Illinois 61801*

(Received 2 June 2009; accepted 8 June 2009; published 31 July 2009)

Electronic systems that offer elastic mechanical responses to high strain deformation are of growing interest due to their ability to enable new applications whose requirements are impossible to satisfy with conventional wafer-based technologies. This article reviews the mechanics of stretchable inorganic materials on compliant substrates. Specifically, three forms of stretchable structures are reviewed. The first one is stretchable ribbon, which provides one-dimensional stretchability. The second is stretchable nanomembranes, which can be stretched in all directions. The last is a noncoplanar mesh design, which has the advantage of providing large stretchability up to and exceeding 100%. Mechanics models and their comparison to experiment are reviewed for these three cases. Such models provide design guidelines for stretchable electronics. © 2009 American Vacuum Society. [DOI: 10.1116/1.3168555]

### I. INTRODUCTION

Realization of electronics with performance equal to established technologies that use rigid semiconductor wafers, but in formats that have the mechanical properties of a rubber band would enable many new application possibilities. Examples include flexible displays,<sup>1</sup> electronic eye camera,<sup>2,3</sup> conformable skin sensors,<sup>4</sup> smart surgical gloves,<sup>5</sup> and structural health monitoring devices.<sup>6</sup> Circuits that use organic semiconductor materials can sustain large deformations,<sup>7–16</sup> but their electrical performance is relatively poor (several orders of magnitude lower than that of conventional inorganic material such as silicon). Compatibility with well developed, high-performance inorganic electronic materials represents a key advantage in this area. The main challenge here is to design inorganic materials (e.g., silicon) for stretchability, which might initially seem challenging since all known inorganic semiconductor materials are brittle and fracture at strains of the order of 1%.

One strategy that avoids directly straining these brittle materials exploits wavy shaped one-dimensional (1D) nanoribbons [Fig. 1(a)] or two-dimensional (2D) nanomembranes [Fig. 1(b)] to make these high-quality, single crystal inor-

ganic semiconductor materials stretchable. The wavy geometry can be realized through nonlinear buckling process in thin films of metal or silicon bonded to prestrained elastomeric poly(dimethylsiloxane) (PDMS) substrates. Different methods have been used to generate the wavy patterns in different film/substrate systems. Bowden *et al.*<sup>17</sup> realized the buckles by depositing thin gold films on a thermally expanded PDMS substrate. Subsequent cooling of the substrate induces compressive force to buckle the film to form waves with 20–50  $\mu\text{m}$ . They observed that the waves can be controlled and oriented by relief structures in the surface of PDMS. Ohzono *et al.*<sup>18</sup> deposited a thin layer of platinum onto hexagonally organized arrays of holes in PDMS and studied the coupling of wrinkle pattern to the PDMS surface structure. They showed that the directional order of buckles was induced when the periodicity of the substrate surface pattern matched the intrinsic wavelength of the buckling. Efimenko *et al.*<sup>19</sup> reported the fabrication of wrinkles by uniaxially stretching the PDMS substrate and exposing it to ultraviolet/ozone (UVO) radiation for a period of time. The UVO treatment converts the topmost  $\sim 5$  nm of the PDMS into a stiff “skin.”<sup>20</sup> After the UVO treatment, the relaxation of stretch forms hierarchical wrinkling pattern with wavelength ranging from a few nanometers to a few millimeters. Recently, Khang *et al.*<sup>21</sup> created wavy Si nanoribbons by transfer printing these nanoribbons from a Si-on-insulator

<sup>a)</sup>Authors to whom correspondence should be addressed; electronic addresses: jsong8@miami.edu and jrogers@illinois.edu

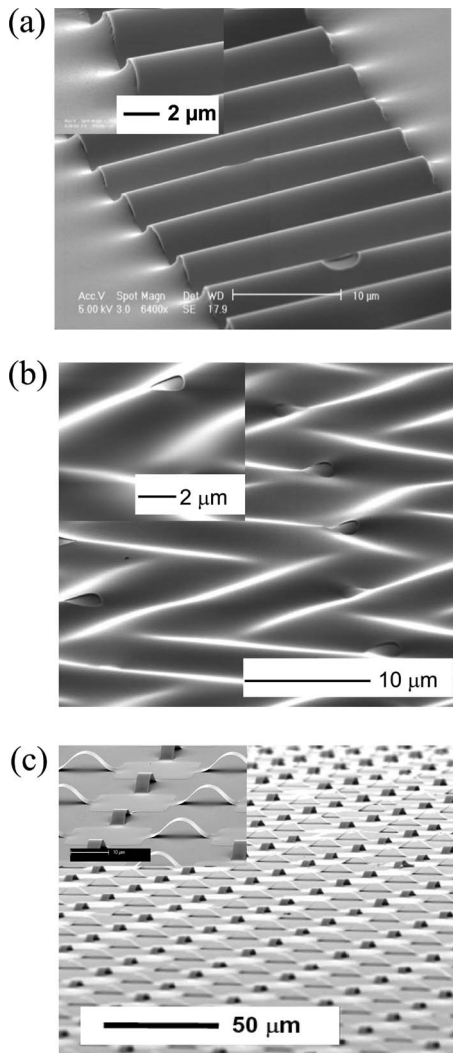


FIG. 1. SEM images of (a) stretchable nanoribbons, (b) stretchable nanomembranes, and (c) noncoplanar mesh design of Si thin film on a compliant substrate.

wafer onto a flat, prestrained PDMS substrate. Releasing the prestrain generates 1D wavy layout. Following the same procedure as Khang *et al.*, Choi *et al.*<sup>22</sup> generated 2D wavy Si nanomembrane. The wavy patterns involved in the above works mainly include 1D sinusoidal wave [Fig. 1(a)] for 1D stretch/compression and ordered (or disordered) herringbone mode [Fig. 1(b)] for 2D stretch/compression. Integrating such stretchable nanoribbons or nanomembranes with dielectrics, patterns of dopants, and thin metal films can generate high-quality, stretchable electronic devices. By using this strategy, Kim *et al.*<sup>23</sup> demonstrated high-performance, stretchable, and foldable integrated circuits (e.g., silicon complementary logic gates, ring oscillators, and different amplifiers). Electronics that use this construction can increase the stretchability up to as high as 30% and are promising especially for applications that involve large coverage of active devices.

The other strategy uses stretchable interconnects such as metal wires to link the rigid device islands (i.e., interconnect-island structure).<sup>2,24–27</sup> Mechanical response to stretching or

compression involves, primarily, deformations only in these interconnects, thereby avoiding unwanted strains in the regions of the active devices. Gray *et al.*<sup>24</sup> and Lacour *et al.*<sup>25</sup> developed coplanar mesh designs by using the wavelike interconnects, which are bonded with the substrate. However, although such coplanar mesh design can improve the stretchability up to around 50%, the stretchability is still too small for certain applications and large scale integration can be difficult.<sup>2,5</sup> Sosin *et al.*<sup>28</sup> showed that freestanding copper interconnects can be used for stretchable electronics and the stretchability can be a few hundred percent. By adopting the “freestanding” idea, Kim *et al.*<sup>27</sup> developed a noncoplanar mesh design [Fig. 1(c)] consisting of device islands linked by “popup” interconnects for stretchable circuits, which can be stretched to rubberlike levels of strain (e.g., up to 100%). Recent work demonstrated a hemispherical electronic eye camera based on this noncoplanar mesh design.<sup>2</sup> Electronics that use this construction are promising especially for applications that involve large stretching and compression.

Figure 1 shows scanning electron micrographs of three main structures for stretchable electronics based on the above strategies. Stretchable nanoribbons, as shown in Fig. 1(a), can be stretched in one direction, while stretchable nanomembranes, as shown in Fig. 1(b), are stretchable in all directions. Figure 1(c) shows a noncoplanar mesh design based on the interconnect-island concept. The details of the fabrication of these three structures will be discussed later in this article.

These systems all exploit mechanics of stiff materials on compliant substrates. This article provides a review of the fundamental aspects of this problem through discussion of theoretical models and their quantitative comparison to experiment. The mechanics of stretchable nanoribbons is described in Sec. II. Theory and results for small pre- and applied strains are presented in Sec. II A, while their counterparts for large strains are given in Sec. II B. Section II C describes the mechanics of local and global buckling of nanoribbons on compliant substrates. Sections II D and II E outline the influence of edges, finite ribbon widths, and spacings, respectively. A method to precisely control the buckling of nanoribbons to achieve large one-dimensional stretchability is presented in Sec. II F. Section III reviews the mechanics of stretchable nanomembranes, where a unique, herringbone two-dimensional buckling patterns can be observed. The relatively new noncoplanar mesh design, optimized for large stretchability, appears in Sec. IV.

## II. MECHANICS OF STRETCHABLE NANORIBBONS

Figure 2 illustrates the fabrication of buckled stiff thin ribbons on compliant substrates,<sup>21</sup> where thin ribbons of single crystal silicon are chemically bonded to flat prestrained elastomeric substrates of PDMS. Releasing the prestrain leads to compressive strains in the ribbons that generate the wavy layouts; these geometries can accommodate external deformations through changes in wavelength and amplitude. The responses of such a structure to applied strain are also shown in Fig. 2.

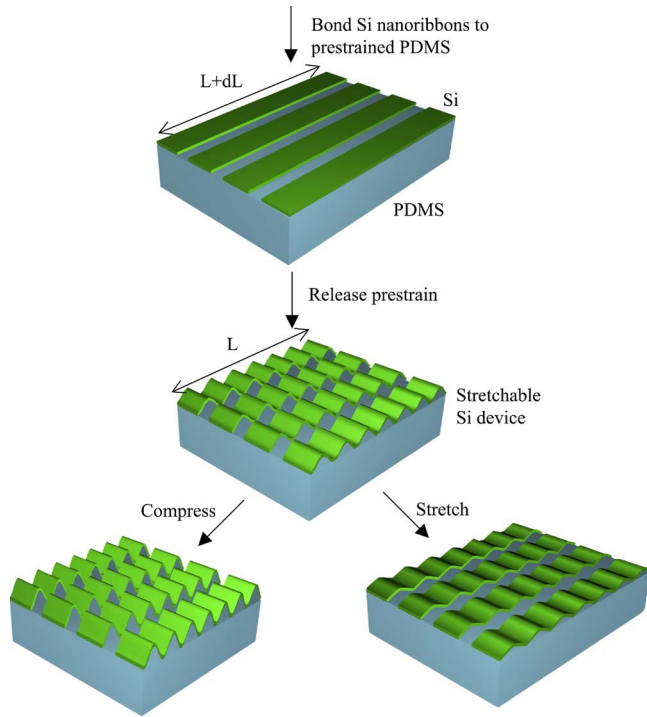


FIG. 2. (Color online) Schematic illustration of the process for fabricating buckled, or wavy, single crystal Si ribbons on a PDMS substrate.

### A. Small-deformation buckling analysis of stiff thin nanoribbons on compliant substrates

We consider a stiff thin film (ribbon) of thickness  $h_f$  and elastic modulus  $E_f$  on a prestretched (prestrain  $\varepsilon_{\text{pre}}$ ), compliant substrate of modulus  $E_s$ , and  $E_f \gg E_s$ . One example is the silicon ribbon ( $E_f = 130$  GPa for the [100] direction of single crystal Si)<sup>29</sup> on a PDMS substrate ( $E_s = 1.8$  MPa) (Ref. 30) with the elastic moduli different by five orders of magnitude. The thin ribbon is modeled as a beam since its thickness ( $\sim 100$  nm) is much smaller than the wavelength of buckled ribbon ( $\sim 10$   $\mu\text{m}$ ). The substrate is linear elastic and is modeled as a semi-infinite solid since it is six orders of magnitude thicker than the thin ribbon. Huang *et al.*<sup>31</sup> developed an energy method based on small-deformation theory to determine the buckling geometry. The total energy consists of three parts, the bending energy  $U_b$  and membrane energy  $U_m$  in the thin film and energy  $U_s$  in the substrate.

The out-of-plane displacement of the buckled thin ribbon can be represented by

$$w = A \cos(kx_1) = A \cos\left(\frac{2\pi x_1}{\lambda}\right), \quad (1)$$

where  $x_1$  is the coordinate along the beam direction, the amplitude  $A$  and wavelength  $\lambda$  (or wave number  $k$ ) are to be determined by energy minimization. The bending energy (the energy expressions in Sec. II and IV are for the structure of a unit width and those in Sec. III are for the structure of a unit area)  $U_b$  can be obtained from Eq. (1) and bending rigidity  $\bar{E}_f h_f^3 / 12$  as

$$U_b = L_0 \frac{1}{\lambda} \int_0^\lambda \frac{\bar{E}_f h_f^3}{24} \left(\frac{d^2 w}{dx^2}\right)^2 dx = \frac{\pi^4 \bar{E}_f h_f^3 A^2}{3\lambda^4} L_0, \quad (2)$$

where  $L_0$ ,  $\bar{E}_f = E_f / (1 - \nu_f^2)$ , and  $\nu_f$  are the length, plane-strain modulus, and Poisson's ratio of thin film, respectively.

The beam undergoes large rotation once the ribbon buckles. The membrane strain  $\varepsilon_{11}$ , which determines the membrane energy in the ribbon, is related to the in-plane displacement  $u_1$  and out-of-plane displacement  $w$  by

$$\varepsilon_{11} = \frac{du_1}{dx_1} + \frac{1}{2} \left(\frac{dw}{dx_1}\right)^2. \quad (3)$$

The membrane force  $N_{11}$  can be related via the plane-strain modulus  $\bar{E}_f$  of the ribbons,

$$N_{11} = \bar{E}_f h_f \varepsilon_{11}. \quad (4)$$

Force equilibrium gives the shear and normal tractions at the ribbon/substrate interface as

$$T_1 = \frac{dN_{11}}{dx_1} \quad (5)$$

and

$$T_3 = -\frac{\bar{E}_f h_f^3}{12} \frac{d^4 w}{dx_1^4} + \frac{d}{dx_1} \left( N_{11} \frac{dw}{dx_1} \right). \quad (6)$$

Huang *et al.*<sup>31</sup> showed that the effect of interface shear is negligible on the buckling of stiff thin ribbon/compliant substrate systems. This leads to  $T_1 = 0$ , which gives the in-plane displacement

$$u_1 = \frac{\pi A^2}{4\lambda} \sin\left(\frac{4\pi x_1}{\lambda}\right) - \varepsilon_{\text{pre}} x_1. \quad (7)$$

The membrane strain then becomes a constant

$$\varepsilon_{11} = \frac{\pi^2 A^2}{\lambda^2} - \varepsilon_{\text{pre}}. \quad (8)$$

The membrane energy  $U_m$  in the film can be obtained by

$$U_m = L_0 \frac{1}{\lambda} \int_0^\lambda \frac{1}{2} N_{11} \varepsilon_{11} dx = \frac{1}{2} \bar{E}_f h_f \left( \frac{\pi^2 A^2}{\lambda^2} - \varepsilon_{\text{pre}} \right)^2 L_0. \quad (9)$$

For a semi-infinite solid subjected to the normal displacement in Eq. (1) and vanishing shear on its boundary, the energy in the substrate is<sup>31</sup>

$$U_s = \frac{\pi}{4\lambda} \bar{E}_s A^2 L_0, \quad (10)$$

where  $\bar{E}_s$  is the plane-strain modulus of the substrate.

The amplitude  $A$  and wavelength  $\lambda$  are then determined by minimizing the total energy  $U_{\text{tot}} = U_m + U_b + U_s$ ,

$$\frac{\partial U_{\text{tot}}}{\partial A} = \frac{\partial U_{\text{tot}}}{\partial \lambda} = 0. \quad (11)$$

This gives a constant wavelength independent of the prestrain and the amplitude

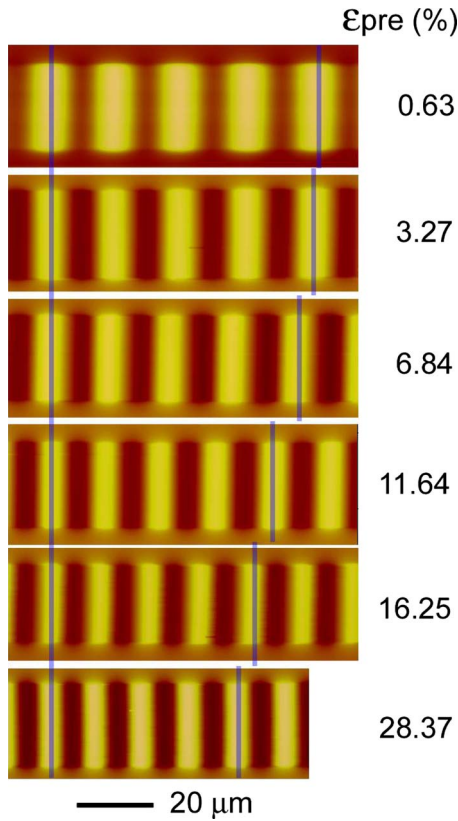


FIG. 3. (Color online) Stacked plane-view AFM images of buckled Si ribbons (100 nm thick) on PDMS for different prestrains. (Reprinted with permission from Ref. 43.)

$$\lambda_0 = 2\pi h_f \left( \frac{\bar{E}_f}{3\bar{E}_s} \right)^{1/3}, \quad A_0 = h_f \sqrt{\frac{\varepsilon_{\text{pre}}}{\varepsilon_c} - 1}, \quad (12)$$

where

$$\varepsilon_c = \frac{1}{4} \left( \frac{3\bar{E}_s}{\bar{E}_f} \right)^{2/3} \quad (13)$$

is the critical strain for buckling, which is 0.034% for the Si ribbon ( $E_f=130$  GPa,  $\nu_f=0.27$ ) (Ref. 29) on PDMS substrate ( $E_s=1.8$  MPa,  $\nu_s=0.48$ ).<sup>30</sup> For  $\varepsilon_{\text{pre}} < \varepsilon_c$ , relaxing the prestrain does not lead to buckling, and therefore there is no bending. Once  $\varepsilon_{\text{pre}} > \varepsilon_c$ , the ribbon buckles such that the membrane strain remains a constant  $\varepsilon_{\text{membrane}} = -\varepsilon_c$  [see Eqs. (8) and (12)] and the bending strain (maximum curvature  $\times h_f/2$ ) increases with the deformation,  $\varepsilon_{\text{bending}} = 2\pi^2/\lambda^2 A h_f$ .

The membrane strain is negligible as compared to the bending strain, and therefore the maximum strain in the ribbon (also called peak strain, which is the sum of membrane and bending strain) can be written as

$$\varepsilon_{\text{peak}} \approx 2\sqrt{\varepsilon_{\text{pre}}\varepsilon_c}. \quad (14)$$

It is much smaller than the prestrain  $\varepsilon_{\text{pre}}$  such that the system can provide large stretchability/compressibility. For example,  $\varepsilon_{\text{peak}}$  is only 1.8% for the system in Fig. 2 when  $\varepsilon_{\text{pre}} = 23.8\%$ .

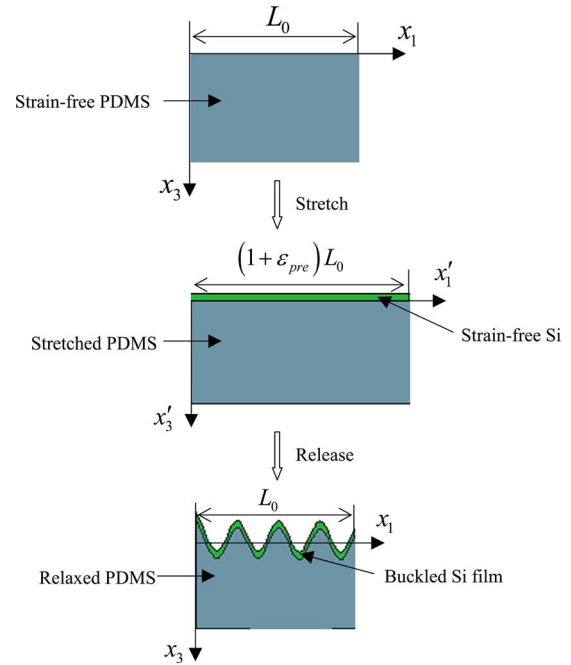


FIG. 4. (Color online) Three sequential configurations for the thin film/substrate buckling process. (Reprinted with permission from Ref. 43.)

For the buckled system subjected to the applied strain  $\varepsilon_{\text{applied}}$ , the above results still hold except that the prestrain  $\varepsilon_{\text{pre}}$  is replaced by  $\varepsilon_{\text{pre}} - \varepsilon_{\text{applied}}$ . The wavelength and amplitude become

$$\lambda = 2\pi h_f \left( \frac{\bar{E}_f}{3\bar{E}_s} \right)^{1/3}, \quad A = h_f \sqrt{\frac{\varepsilon_{\text{pre}} - \varepsilon_{\text{applied}}}{\varepsilon_c} - 1}. \quad (15)$$

The membrane strain remains at  $-\varepsilon_c$ , and the bending strain becomes  $2\sqrt{(\varepsilon_{\text{pre}} - \varepsilon_{\text{applied}})\varepsilon_c}$ . The peak strain in the ribbon can be written as

$$\varepsilon_{\text{peak}} \approx 2\sqrt{(\varepsilon_{\text{pre}} - \varepsilon_{\text{applied}})\varepsilon_c}. \quad (16)$$

## B. Finite-deformation buckling analysis of stiff thin nanoribbons on compliant substrates

Section II A predicts a constant wavelength, independent of the prestrain or applied strain [see Eqs. (12) and (15)]. This result has been widely used in high precision micro- and nanometrology methods<sup>30,32,33</sup> and pattern formation for micro-/nanofabrication.<sup>17,34–39</sup> However, recent experiments in Si/PDMS,<sup>21,40</sup> polystyrene/PDMS,<sup>41</sup> and platinum/rubber<sup>42</sup> systems at large strains show that the wavelength decreases with increasing prestrain, as illustrated in Fig. 3 for the Si/PDMS system.

Jiang *et al.*<sup>40</sup> and Song *et al.*<sup>43</sup> pointed out that the strain-dependent wavelength is due to the finite deformation (i.e., large strain) in the compliant substrate and established a buckling theory that accounts for finite deformations to yield a quantitatively accurate description of the system. The analysis is different from all previous buckling analyses in the following three aspects.

- (i) Finite geometry change. The initial strain-free (or stress-free) states are different for the PDMS substrate and Si thin ribbon. This aspect is further illustrated in Fig. 4. The top figure shows the strain-free state of the PDMS with the original length  $L_0$ . The middle figure shows the stretched PDMS attached to a strain-free Si thin ribbon with the original length  $(1 + \varepsilon_{\text{pre}})L_0$ . Releasing the prestrain buckles the Si ribbon, as illustrated at the bottom figure.
- (ii) Finite strain. The strain-displacement relation in the PDMS substrate becomes nonlinear at large prestrain.
- (iii) Constitutive model. The stress-strain relation in the PDMS substrate becomes nonlinear at the large prestrain.

The out-of-plane displacement of the buckled thin ribbon can be represented by

$$w = A \cos\left(\frac{2\pi x_1}{\lambda}\right) = A \cos\left[\frac{2\pi x'_1}{(1 + \varepsilon_{\text{pre}})\lambda}\right], \quad (17)$$

where the coordinate  $x'_1$  in the relaxed configuration and  $x_1$  in the strain-free configuration are related by  $x'_1 = (1 + \varepsilon_{\text{pre}})x_1$ .

The thin ribbon is still modeled as a beam. The governing equations for the thin ribbon [Eqs. (2)–(9)] still hold except that the coordinate  $x_1$  is replaced by  $x'_1$ . The bending energy  $U_b$  is given by

$$U_b = \frac{\pi^4}{3} \frac{\bar{E}_f h_f^3 A^2}{[(1 + \varepsilon_{\text{pre}})\lambda]^4} (1 + \varepsilon_{\text{pre}})L_0, \quad (18)$$

where  $(1 + \varepsilon_{\text{pre}})L_0$  is the initial length of strain-free Si thin ribbon (Fig. 4, middle figure).

The membrane strain in Eq. (3) now becomes

$$\varepsilon_{11} = \frac{du_1}{dx'_1} + \frac{1}{2} \left( \frac{dw}{dx'_1} \right)^2. \quad (19)$$

The neglect of interface shear gives the in-plane displacement

$$u_1 = \frac{\pi A^2}{4(1 + \varepsilon_{\text{pre}})\lambda} \sin\left[\frac{4\pi x'_1}{(1 + \varepsilon_{\text{pre}})\lambda}\right] - \frac{\varepsilon_{\text{pre}}}{1 + \varepsilon_{\text{pre}}} x'_1. \quad (20)$$

The membrane strain becomes

$$\varepsilon_{11} = \frac{\pi^2 A^2}{(1 + \varepsilon_{\text{pre}})^2 \lambda^2} - \frac{\varepsilon_{\text{pre}}}{1 + \varepsilon_{\text{pre}}}. \quad (21)$$

The membrane energy  $U_m$  is given by

$$U_m = \frac{1}{2} \bar{E}_f h_f \left[ \frac{\pi^2 A^2}{(1 + \varepsilon_{\text{pre}})^2 \lambda^2} - \frac{\varepsilon_{\text{pre}}}{1 + \varepsilon_{\text{pre}}} \right]^2 (1 + \varepsilon_{\text{pre}})L_0. \quad (22)$$

The substrate is modeled as a nonlinear elastic semi-infinite solid by accounting the geometric and material nonlinearity. For large stretch, the Green strains  $E_{IJ}$  in the substrate are related to the displacements as

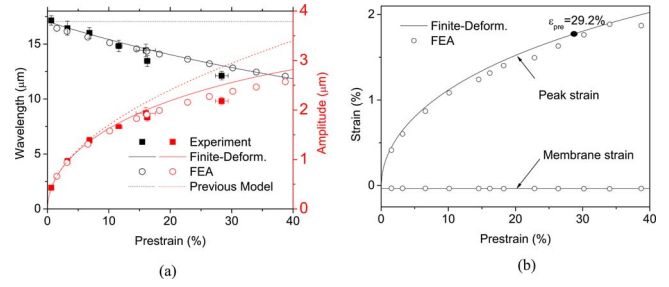


FIG. 5. (Color online) (a) Wavelength and amplitude (b) membrane and peak strains of buckled Si ribbons (100 nm thick) on PDMS as a function of the prestrain. (Reprinted with permission from Ref. 43.)

$$E_{IJ} = \frac{1}{2} \left( \frac{\partial u_I}{\partial x_J} + \frac{\partial u_J}{\partial x_I} + \frac{\partial u_K}{\partial x_I} \frac{\partial u_K}{\partial x_J} \right), \quad (23)$$

where the subscripts  $I$  and  $J$  are 1 or 3. The neo-Hookean constitutive law is used to represent the substrate, which gives the nonlinear elastic constitutive relation<sup>43,44</sup>

$$T_{IJ} = T_{IJ}(E_{KL}), \quad (24)$$

where  $T_{IJ}$  is the second Piola–Kirchhoff stress. The force equilibrium equation for finite deformation is

$$(F_{iK} T_{JK})_{,J} = 0, \quad (25)$$

where  $F_{iK}$  is the deformation gradient.

Song *et al.*<sup>43</sup> obtained the analytical solution for Eqs. (23)–(25) by using perturbation method and gave the strain energy in the substrate as

$$U_s = \frac{\pi E_s A^2}{3} \left( 1 + \frac{5}{32} \frac{\pi^2 A^2}{\lambda^2} \right) L_0, \quad (26)$$

where  $L_0$  is the original length of the substrate.

Minimization of the total energy (sum of the membrane and bending energy in the thin ribbon and the strain energy in the substrate) gives the wavelength and amplitude

$$\lambda = \frac{\lambda_0}{(1 + \varepsilon_{\text{pre}})(1 + \xi)^{1/3}}, \quad A \approx \frac{A_0}{\sqrt{1 + \varepsilon_{\text{pre}}(1 + \xi)^{1/3}}}, \quad (27)$$

where  $\lambda_0$  and  $A_0$  are the wavelength and amplitude in Eq. (12) based on the small-deformation theory, and  $\xi = 5\varepsilon_{\text{pre}}(1 + \varepsilon_{\text{pre}})/32$ . As shown in Fig. 5(a), both the wavelength and amplitude agree well with the experimental data without any parameter fitting. Contrary to the small-deformation theory, the wavelength  $\lambda$  given by the finite-deformation theory is strain dependent, and it approaches  $\lambda_0$  at the limit of vanishing strain.

Song *et al.*<sup>43</sup> also developed a finite element model to study the buckling of stiff thin ribbon on compliant substrate. The Si thin ribbon is modeled by the beam elements and the substrate by the 4-node plane-strain elements. The Si ribbon is bonded to the prestretched substrate by sharing the same nodes at the interface. As shown in Fig. 5(a), the numerical results from finite element analysis (FEA) agree well with the experimental data and the analytical solution.

The membrane strain is then obtained from Eq. (21) as

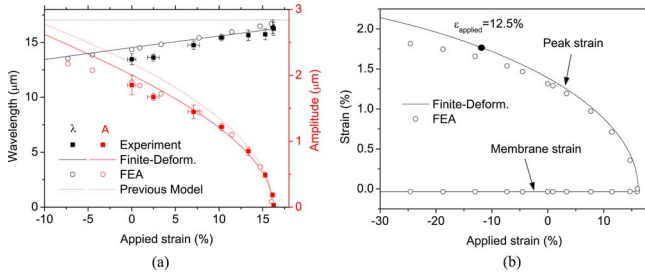


FIG. 6. (Color online) (a) Wavelength and amplitude and (b) membrane and peak strains of buckled Si ribbons (100 nm thick) on PDMS formed with a prestrain of 16.2% as a function of the applied strain. (Reprinted with permission from Ref. 43.)

$$\varepsilon_{\text{membrane}} = -\frac{1 + \frac{\xi}{3}}{(1 + \xi)^{1/3}} \varepsilon_c,$$

which remains essentially a constant,  $-\varepsilon_c$ , for the prestrain up to 100%. The bending strain in the buckled ribbon is

$$\varepsilon_{\text{bending}} = 2(1 + \xi)^{1/3} \sqrt{\varepsilon_c} \sqrt{\frac{\varepsilon_{\text{pre}}}{1 + \varepsilon_{\text{pre}}} - \frac{1 + \frac{\xi}{3}}{(1 + \xi)^{1/3}} \varepsilon_c}.$$

The peak strain (sum of membrane and bending strain) can be approximately by

$$\varepsilon_{\text{peak}} \approx 2\sqrt{\varepsilon_{\text{pre}} \varepsilon_c} \frac{(1 + \xi)^{1/3}}{\sqrt{1 + \varepsilon_{\text{pre}}}}. \quad (28)$$

Figure 5(b) shows  $\varepsilon_{\text{peak}}$  and  $\varepsilon_{\text{membrane}}$  versus  $\varepsilon_{\text{pre}}$ . Both the membrane and peak strains agree well with FEA. The membrane strain remains essentially a constant and is negligible compared to the peak strain. The peak strain is much smaller than the prestrain, such that the system can accommodate large strains. The maximum allowable prestrain is determined by  $\varepsilon_{\text{peak}} = \varepsilon_{\text{fracture}}$  as

$$\frac{\varepsilon_{\text{fracture}}^2}{4\varepsilon_c} \left( 1 + \frac{43}{48} \frac{\varepsilon_{\text{fracture}}^2}{4\varepsilon_c} \right),$$

where  $\varepsilon_{\text{fracture}}$  is the fracture strain. For Si with  $\varepsilon_{\text{fracture}} = 1.8\%$ , the maximum allowable prestrain is  $\sim 29\%$ , which is almost 20 times larger than  $\varepsilon_{\text{fracture}}$ .

For the system subjected to applied strain after buckling, Song *et al.*<sup>43</sup> obtained the membrane and bending energy in the thin ribbon and the strain energy in the substrate in terms of the prestrain and the applied strain. The minimization of the total energy gives the wavelength and amplitude

$$\lambda'' = \frac{\lambda_0(1 + \varepsilon_{\text{applied}})}{(1 + \varepsilon_{\text{pre}})(1 + \varepsilon_{\text{applied}} + \zeta)^{1/3}},$$

$$A'' \approx h_f \frac{\sqrt{(\varepsilon_{\text{pre}} - \varepsilon_{\text{applied}})/\varepsilon_c - 1}}{\sqrt{1 + \varepsilon_{\text{pre}}(1 + \varepsilon_{\text{applied}} + \zeta)^{1/3}}}, \quad (29)$$

where  $\zeta = 5(\varepsilon_{\text{pre}} - \varepsilon_{\text{applied}})(1 + \varepsilon_{\text{pre}})/32$ . As shown in Fig. 6(a) for a buckled Si thin ribbon/PDMS substrate system formed

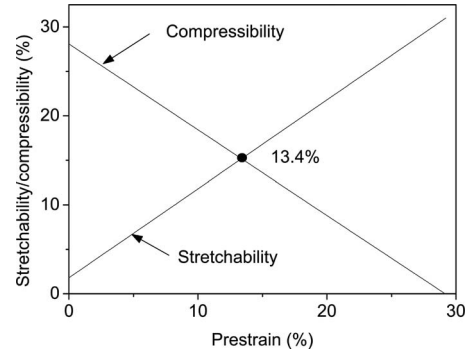


FIG. 7. Analytically predicted stretchability and compressibility of buckled Si ribbons (100 nm thick) on PDMS. (Reprinted with permission from Ref. 43.)

at the prestrain of 16.2%, both amplitude and wavelength agree well with the experimental data and numerical results from FEA. The wavelength increases with the applied strain, and the amplitude decreases and becomes zero once the applied strain reaches  $\varepsilon_{\text{pre}} - \varepsilon_c$  such that the thin film becomes flat. Further increase in the applied strain leads to stretching of the flat thin film which has no bending. The strain in the thin film reaches zero and the fracture strain  $\varepsilon_{\text{fracture}}$  as the applied strain reaches  $\varepsilon_{\text{pre}}$  and  $\varepsilon_{\text{pre}} + \varepsilon_{\text{fracture}}$ , respectively. Therefore the stretchability (maximum applied tensile strain) is  $\varepsilon_{\text{pre}} + \varepsilon_{\text{fracture}}$ , which varies linearly with the prestrain.

The membrane and peak strain in the ribbon are obtained as

$$\varepsilon_{\text{membrane}} \approx -\varepsilon_c,$$

$$\varepsilon_{\text{peak}} \approx 2\sqrt{(\varepsilon_{\text{pre}} - \varepsilon_{\text{applied}})\varepsilon_c} \frac{(1 + \varepsilon_{\text{applied}} + \xi)^{1/3}}{\sqrt{1 + \varepsilon_{\text{pre}}}}, \quad (30)$$

before the applied strain reaches  $\varepsilon_{\text{pre}} - \varepsilon_c$ . Figure 6(b) shows  $\varepsilon_{\text{peak}}$  and  $\varepsilon_{\text{mem}}$  as a function of  $\varepsilon_{\text{applied}}$ . Both membrane and peak strain agree well with finite element analysis. The compressibility is the maximum applied compressive strain when the peak Si strain reaches  $\varepsilon_{\text{fracture}}$  and it is well approximated by

$$\frac{\varepsilon_{\text{fracture}}^2}{4\varepsilon_c} \left( 1 + \frac{43}{48} \frac{\varepsilon_{\text{fracture}}^2}{4\varepsilon_c} \right) - \varepsilon_{\text{pre}}.$$

For Si with  $\varepsilon_{\text{fracture}} = 1.8\%$ , the compressibility is  $\sim 12.5\%$ . Figure 7 shows the stretchability and compressibility versus the prestrain. The stretchability increases with the prestrain but the compressibility decreases. The Si/PDMS system has equal stretchability and compressibility when the prestrain is 13.4%.

### C. Local versus global buckling of stiff thin nanoribbons on compliant substrates

Sections II A and II B discussed the occurrence of the local buckling pattern [Fig. 2 or Fig. 8(b)] to generate stretchable nanoribbons. The critical buckling strain is given by

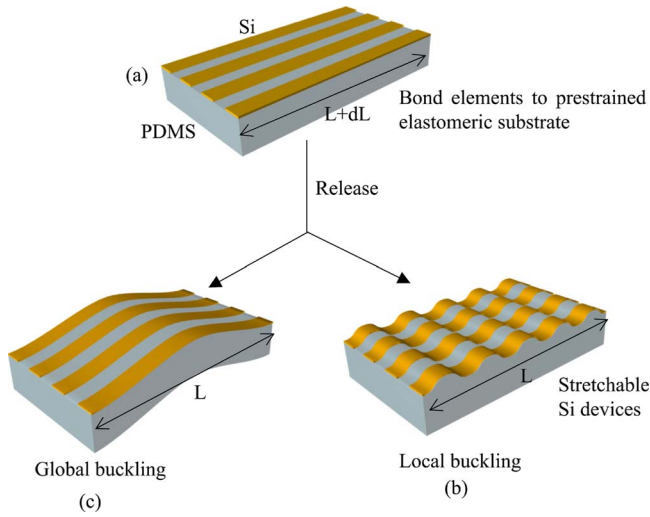


FIG. 8. (Color online) Schematic illustration of the process for fabricating buckled single crystal Si ribbons (yellow) on a PDMS (gray) substrate; (a) bond Si elements to prestretched PDMS; (b) local buckling; and (c) global buckling due to release of prestretch. (Reprinted with permission from Ref. 45)

$$\varepsilon_{\text{critical}}^{\text{local}} = \frac{1}{4} \left( \frac{3\bar{E}_s}{\bar{E}_f} \right)^{2/3}, \quad (31)$$

which only depends on the elastic moduli of the film and substrate. The substrate thickness  $h_s$  does not come into play because the substrate is much thicker than the film and is therefore considered as a semi-infinite solid. For a relatively thin substrate, local buckling mode does not occur. Instead, the global buckling mode shown in Fig. 8(c) has been observed in experiments. It is important to identify the critical condition separating the local and global buckling modes for an elastic film on an elastomeric substrate to ensure system design that leads to local buckling. Wang *et al.*<sup>45</sup> compared the critical local buckling strain  $\varepsilon_{\text{critical}}^{\text{local}}$  in Eq. (31) with the critical global buckling strain, to be given in the following, to determine the critical condition separating the two buckling modes.

In global buckling, the film and the substrate are modeled as a composite beam with the effective tensile rigidity  $EA = \bar{E}_s h_s + \bar{E}_f h_f$  and bending rigidity

$$\frac{EI}{EI} = \frac{(\bar{E}_f h_f^2 - \bar{E}_s h_s^2) + 4\bar{E}_f h_f \bar{E}_s h_s (h_f + h_s)^2}{12(\bar{E}_f h_f + \bar{E}_s h_s)}.$$

For a beam with clamped ends and length  $L$  and rectangular cross section, the critical buckling strain by accounting the shear effect is<sup>46</sup>

$$\varepsilon_{\text{critical}}^{\text{global}} = \frac{1}{1 + \frac{4.8\pi^2 EI/L^2}{\bar{G}(h_s + h_f)}} \frac{4\pi^2 \bar{E} I/L^2}{EA}, \quad (32)$$

where  $\bar{G}$  is the effective shear modulus of the composite beam, which is approximately the shear modulus  $G_s$  of the

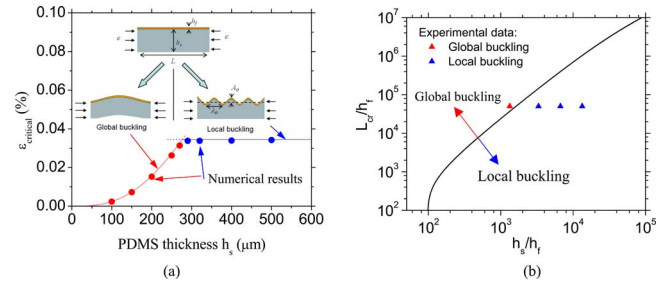


FIG. 9. (Color online) (a) Critical strains of one-dimensional local and global buckling vs substrate thickness  $h_s$  for the Si/PDMS system with  $h_f = 1 \mu\text{m}$  and  $L = 3 \text{ mm}$ . (b) Critical condition of one-dimensional local and global buckling for the Si/PDMS system. (Reprinted with permission from Ref. 45.)

substrate since the film is very stiff ( $E_f \gg E_s$ ) and thin ( $h_f \ll h_s$ ).

Figure 9(a) shows the critical local and global buckling strains from Eqs. (31) and (32) versus the substrate thickness  $h_s$  for a  $1 \mu\text{m}$ -thick- and 3-mm-long Si film on a PDMS substrate. The red curve is for the global buckling strain, which increases with the substrate thickness, while the blue curve is for the local buckling strain, which remains a constant,  $\sim 0.034\%$ . Global buckling occurs for a small substrate thickness such that  $\varepsilon_{\text{critical}}^{\text{local}} > \varepsilon_{\text{critical}}^{\text{global}}$ , while local buckling occurs for a thick substrate (i.e.,  $\varepsilon_{\text{critical}}^{\text{local}} > \varepsilon_{\text{critical}}^{\text{global}}$ ). The condition  $\varepsilon_{\text{critical}}^{\text{local}} = \varepsilon_{\text{critical}}^{\text{global}}$  gives the critical condition to separate the two buckling modes. Wang *et al.*<sup>45</sup> also developed a finite element model to verify the above criterion for local and global buckling strain. The film is modeled by beam elements and the substrate by solid elements. The blue dots in Fig. 9(a) are the numerical results for local buckling and the red dots for global buckling. Good agreement with the analytical expressions (31) and (32) has been observed.

The critical length  $L_{\text{critical}}$  separating local and global buckling can be obtained as

$$L_{\text{critical}} = 4\pi \sqrt{\frac{EI}{\left[ \frac{[\bar{E}_f/3\bar{E}_s]^{2/3}}{\bar{E}_s h_s + \bar{E}_f h_f} - \frac{0.3}{G_s (h_f + h_s)} \right]}} \quad (33)$$

from  $\varepsilon_{\text{critical}}^{\text{local}} = \varepsilon_{\text{critical}}^{\text{global}}$ . Local and global bucklings occur for  $L < L_{\text{critical}}$  and  $L > L_{\text{critical}}$ , respectively. Figure 9(b) shows the critical length normalized by film thickness,  $L_{\text{critical}}/h_f$ , versus the ratio of substrate to film thickness,  $h_s/h_f$ , for the Si film on PDMS substrate. This curve separates local buckling from global buckling. Local buckling occurs below the curve, while global buckling occurs above the curve. Figure 9(b) also shows the experimental results (solid triangular) for film thickness of  $h_f = 300 \text{ nm}$ , length of  $L = 15 \text{ mm}$ , and several substrate thicknesses of  $h_s = 0.4, 0.6, 1.0, 2.0,$  and  $4.0 \text{ mm}$ . Global buckling is observed for  $h_s = 0.4 \text{ mm}$  and local buckling for all other cases. Figure 9(b) predicts a critical substrate thickness of  $h_s = 0.51 \text{ mm}$  separating the local and global bucklings for  $h_f = 300 \text{ nm}$  and  $L = 15 \text{ mm}$  as in experiments. Global buckling occurs for  $h_s < 0.51 \text{ mm}$ , while local buckling occurs for  $h_s > 0.51$ . The analytical prediction

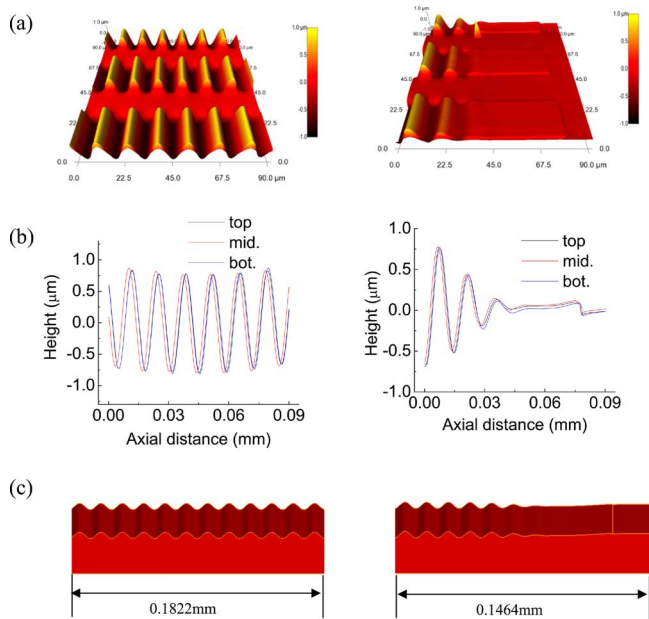


FIG. 10. (Color online) (a) Images and (b) line cuts of atomic force micrographs and (c) finite element results of buckled single crystal Si ribbons on PDMS substrate. The images in the left and right columns are for the center part and edge of the Si thin film, respectively. (Reprinted with permission from Ref. 47.)

for the case of  $h_f=300$  nm and  $L=15$  mm agrees well with the experimental observations: global buckling for  $h_s=0.4$  mm and local buckling for  $h_s=0.6, 1.0, 2.0,$  and  $4.0$  mm.

#### D. Edge effect

Buckled thin films on elastomeric substrates exhibit periodic sinusoidal wavy layouts except near the edges. In these regions, the amplitude of the waves decreases until the film becomes flat. Figure 10 clearly shows these features for 100-nm-thick ribbons of Si bonded to a 3.5-mm-thick PDMS substrate.<sup>47</sup> The images and line cuts on the left correspond to periodic structures for the regions far away from the free edge, while those on the right correspond to regions near the free edge. Koh *et al.*<sup>47</sup> developed a finite element model to study the mechanics of this phenomenon. The bottom images [Fig. 10(c)] are obtained from finite element analysis, as described in the following.

The thin film and the substrate are modeled by beam and plane-strain elements, respectively. The modeled two-dimensional system consists of a 1.3-mm-long and 3.5-mm-thick PDMS substrate. The length 1.3 mm is about two orders of magnitude larger than both the wavelength and length of the flat region (a few tens of micrometers), which is sufficiently long to represent the edge effect. Once the substrate is stretched  $\epsilon_{\text{pre}}$ , a shorter 1 mm-long- and 100-nm-thick Si thin ribbon is attached to the top surface of the stretched PDMS substrate by sharing the nodes at the interface. It should be noticed that only the center part of the substrate surface is covered by the Si ribbon because the substrate length (1.3 mm) is longer than that of Si ribbon (1 mm).

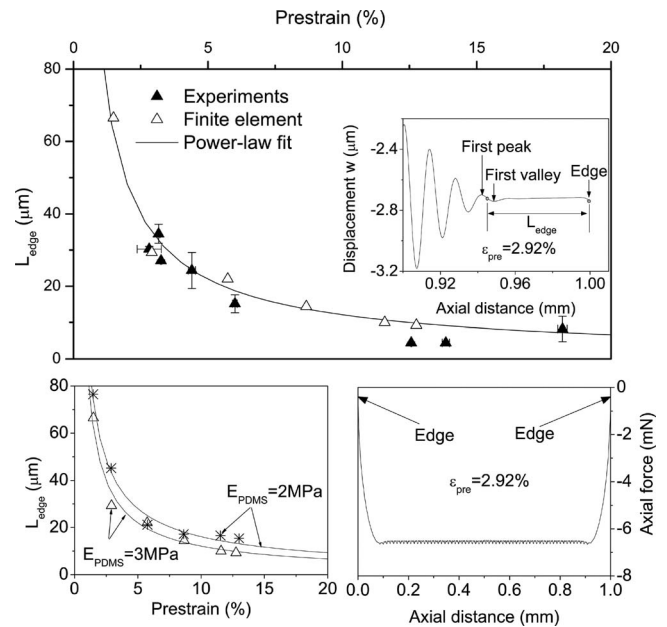


FIG. 11. Edge-effect length  $L_{\text{edge}}$  vs prestrain for Young's modulus of 3 MPa of the PDMS substrate (top panel); its inset gives the definition of  $L_{\text{edge}}$ ; the edge-effect length is shown at the bottom left panel for Young's moduli of 2 and 3 MPa of the PDMS substrate; the distribution of axial force in the Si thin film is shown at the bottom right panel. (Reprinted with permission from Ref. 47.)

The edge-effect length  $L_{\text{edge}}$  denotes the size of the flat region near edges and it is defined as the distance from the edge to the midpoint between the first peak and valley nearest to the free edge (Fig. 11, top inset). The top frame in Fig. 11 clearly shows the experimentally measured  $L_{\text{edge}}$  agrees well with the numerical results. The bottom left panel in Fig. 11 shows the substrate modulus effect on the edge-effect length  $L_{\text{edge}}$ . The edge-effect length increases as the substrate modulus decreases since  $L_{\text{edge}}$  for  $E_s=2$  MPa is larger than that for 3 MPa.

The bottom right panel in Fig. 11 shows the distribution of the axial force in the buckled thin ribbon, which explains the edge effect. Except near the edges, the axial force in the thin ribbon is a constant, which is equal to the membrane strain (i.e., critical strain  $\epsilon_c$ ) in Eq. (13) multiplied by the tensile rigidity  $\bar{E}_f h_f$  of the ribbon. Near the edges, this constant force decreases and becomes zero at the free edges, which explains why the ribbon in these regions does not buckle. Therefore, the traction-free boundary results in the flat region of the thin ribbon.

#### E. Ribbon width and spacing effect

The analyses in the above sections involve an assumption that the thin ribbon width (the dimension perpendicular to the prestrain direction) is much larger than the wavelength, and therefore the deformation is assumed to be plane strain. This assumption, however, does not hold in many applications, such as the stripedlike thin ribbon in stretchable metal interconnects.

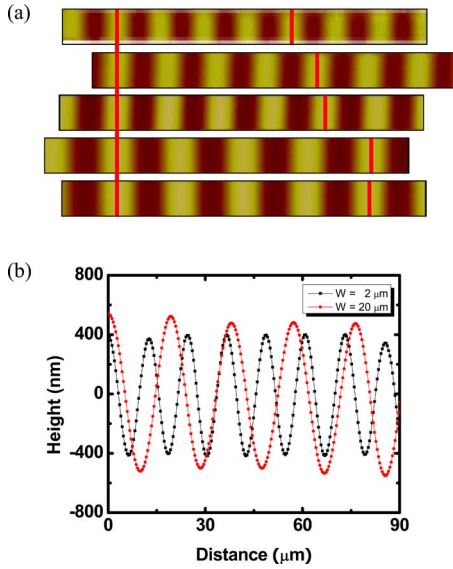


FIG. 12. (Color online) (a) Stacked plane-view AFM images of buckled Si ribbons having different widths of 2, 5, 20, 50, and 100  $\mu\text{m}$  (from top to bottom). (b) AFM line cut profiles along the buckled wavy Si ribbons for 2  $\mu\text{m}$  (black) and 20  $\mu\text{m}$  (red) wide ribbons. (Reprinted with permission from Ref. 48.)

The strong effect of the ribbon width for the Si/PDMS system is shown in Fig. 12. For better visualization and comparison, plane-view AFM images of Si ribbons with different widths (2, 5, 20, 50, and 100  $\mu\text{m}$ , from top to bottom) are stacked together in Fig. 12(a). The long and short vertical red lines define the relative peak locations on each ribbon. It clearly shows that the wavelength increases with the ribbon width and then seems to saturate when the ribbon width reaches a finite value. The line cut profiles for the 2 and 20  $\mu\text{m}$  wide ribbons are shown in Fig. 12(b). The data are shifted to make the peaks coincide, thereby making it easy to observe that the buckling amplitude and wavelength increase with the ribbon width, i.e., a strong ribbon width effect.

Jiang *et al.*<sup>48</sup> obtained the analytical solution for the buckling of a finite-width stiff ribbon on a compliant substrate, shown schematically in Fig. 13(a). The ribbon is modeled as a beam such that the bending energy in Eq. (2) and membrane energy in Eq. (9) still hold except that they need to be multiplied by the ribbon width  $W$ . The substrate is modeled as a three-dimensional (3D) semi-infinite solid with traction-free surface except for the portion underneath the ribbon. The strain energy in the substrate can be expressed analytically as

$$U_s = \frac{1}{\pi \bar{E}_s} \left[ E_f k h_f A \left( \frac{1}{12} k^2 h_f^2 + \frac{1}{4} A^2 k^2 - \varepsilon_{\text{pre}} \right) \right]^2 \rho(Wk), \quad (34)$$

where

$$\rho(x) = -1 + xY_1(x) + x^2Y_0(x) + \frac{\pi}{2} x^2 [H_1(x)Y_0(x) + H_0(x)Y_1(x)] \quad (35)$$

is a nondimensional function,  $Y_n$  ( $n=0, 1, 2, \dots$ ) is the Bessel

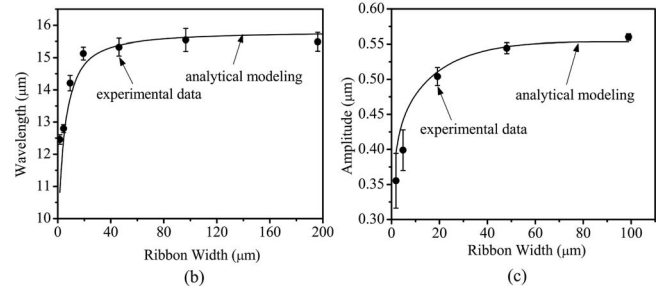
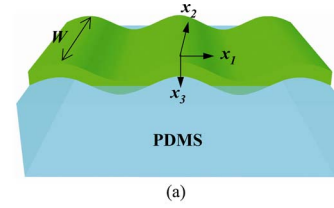


FIG. 13. (Color online) (a) Schematic illustration of the geometry and coordinate system for a buckled single thin film on PDMS substrate.  $W$  is the width of the thin film. (b) Wavelength and (c) amplitude of the buckling profile as a function of the width of silicon thin films. The theoretical analysis is shown in solid line and the experimental data is shown in filled circles. (Reprinted with permission from Ref. 48.)

function of the second kind, and  $H_n$  ( $n=0, 1, 2, \dots$ ) denotes the Struve function.<sup>49</sup>

The energy minimization is employed to obtain the following governing equation for the wave number  $k$ :

$$\frac{\bar{E}_s W^3}{E_f h_f^3} = \frac{2}{3\pi} \frac{W^2 k^2 [\rho(Wk)]^2}{\rho(Wk) + 1 - WkY_1(Wk)}. \quad (36)$$

By rearranging the above equation, the wave number  $k$  was found to depend on the ribbon and substrate elastic moduli and film thickness  $h_f$  and width  $W$  through a nondimensional function  $f$ ,

$$k = \frac{1}{h_f} \left( \frac{3\bar{E}_s}{E_f} \right)^{1/3} f \left[ \left( \frac{\bar{E}_s}{E_f} \right)^{1/3} \frac{W}{h_f} \right]. \quad (37)$$

The nondimensional  $f$  of its variable  $(\bar{E}_s/E_f)^{1/3} W/h_f$  is determined numerically from Eq. (36), which can be well approximated by the simple relation<sup>48</sup>  $f(x) \approx \coth(16/15x^{1/4})$ . Therefore, the wavelength  $\lambda = 2\pi/k$  can be obtained as

$$\lambda = 2\pi h_f \left( \frac{E_f}{3\bar{E}_s} \right)^{1/3} \tanh \left\{ \frac{16}{15} \left[ \left( \frac{\bar{E}_s}{E_f} \right)^{1/3} \frac{W}{h_f} \right]^{1/4} \right\}, \quad (38)$$

which suggests that the wavelength depends on the film width  $W$  through the nondimensional combination  $(\bar{E}_s/E_f)^{1/3} W/h_f$ .

The energy minimization also gives the amplitude as

$$A = \begin{cases} \frac{2}{k} \sqrt{\varepsilon_{\text{pre}} - F}, & \varepsilon_{\text{pre}} \geq F \\ 0, & \varepsilon_{\text{pre}} < F, \end{cases} \quad (39)$$

where

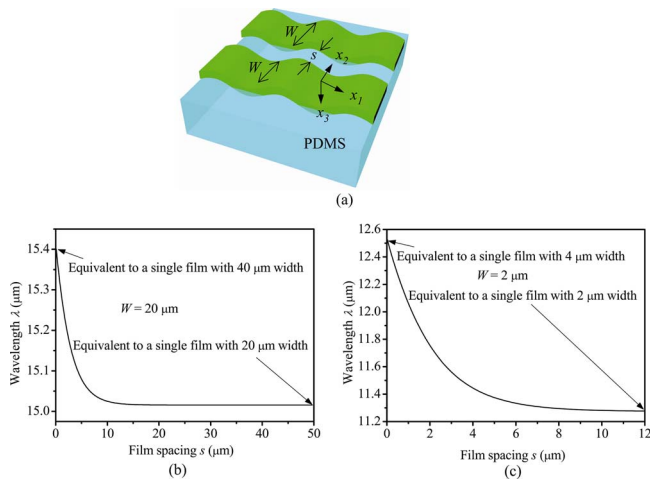


FIG. 14. (Color online) (a) Schematic illustration of the geometry and coordinate system for two buckled thin films on PDMS substrate with identical thickness and width  $W$ .  $s$  is the spacing between two thin films. The predicted buckling wavelength from Eq. (41) as a function of spacing  $s$  between two thin films with identical widths of 20  $\mu\text{m}$  (b) and 2  $\mu\text{m}$  (c). (Reprinted with permission from Ref. 48.)

$$F = \frac{\pi W \bar{E}_s}{4h_f E_f \rho(Wk)} + \frac{1}{12} h_f^2 k^2. \quad (40)$$

Figures 13(b) and 13(c) compare the ribbon wide-dependent buckling wavelength and amplitude given by Eqs. (38) and (39) (solid line) with the experimental results (filled circles), respectively. The thickness of the Si ribbon is 100 nm and the prestrain is 1.3%. The analytical solution agrees very well with experiments and it clearly shows that the buckling profile depends strongly on the film width. For example, the buckling wavelength varies from 15.5  $\mu\text{m}$  for 100- $\mu\text{m}$ -wide ribbon to 12.5  $\mu\text{m}$  for 2- $\mu\text{m}$ -wide ribbon.

Jiang *et al.*<sup>48</sup> also obtained an analytical solution for the effect of ribbon spacing, which is studied via the model of two ribbons with the same thickness  $h_f$  and width  $W$  shown schematically in Fig. 14(a). The ribbon spacing is denoted by  $s$ . The wavelength and amplitude can be obtained by energy minimization. Specifically, the wave number  $k$  is determined by the following nonlinear equation:

$$\frac{1}{3\pi} + \frac{E_s W}{k E_f h_f^3} \frac{d}{dk} \times \left\{ \frac{1}{2\rho(wk) + \rho(sk) - 2\rho[(W+s)k] + \rho[(2W+s)k]} \right\} = 0, \quad (41)$$

where the function  $\rho$  is given in Eq. (35). Figures 14(b) and 14(c) show the wavelength  $\lambda$  versus the ribbon spacing  $s$  for two moderately wide ribbons (width of  $W=20 \mu\text{m}$ ) and two narrow ribbons (width of  $W=2 \mu\text{m}$ ). For the limit of ribbon spacing  $s$  approaching infinity, the two ribbons buckle independently, and the wavelength becomes that for a single ribbon of width  $W$ . For the other limit of  $s$  approaching to zero, the two ribbons have strong interactions and they buckle together with the same wavelength as that of width  $2W$ . For

moderately wide ribbons ( $W=20 \mu\text{m}$ ), the effect of ribbon spacing is almost negligible since the wavelength varies only 2% for the two limits of ribbon spacing. For narrow ribbons ( $W=2 \mu\text{m}$ ), the effect of ribbon spacing is significant with 12% changes for the two limits of ribbon spacing. The spacing effect disappears when the ribbon spacing reaches about three times the width (i.e., 6  $\mu\text{m}$ ).

## F. Precisely controlled buckling of stiff thin nanoribbons on compliant substrates

The approach discussed in prior sections has the following limitations.

- (1) The buckling profile of the “wavy” Si ribbons is determined by material properties (e.g., moduli and thickness) without any direct control over the geometries.
- (2) The stretchability is still too small for certain applications although the range of acceptable strain is improved significantly (to  $\sim 20\%$ ) compared to that of silicon itself ( $\sim 1\%$ ).

To control the buckle geometries and improve the stretchability, the precisely controlled buckle geometries for nanoribbons of GaAs and Si was developed by Sun *et al.*<sup>50</sup> via a combined lithographically patterned surface bonding chemistry and a buckling process similar to that reported in Khang *et al.*<sup>21</sup>

The fabrication procedure is illustrated in Figs. 15(a)–15(c). Figure 15(a) shows the photolithography process that defines the bonding chemistry on a prestretched PDMS substrate with prestrain  $\varepsilon_{\text{pre}} = \Delta L/L$ . The patterning process creates selected regions with activated sites where chemical bonding occurs between the ribbons (GaAs or Si) and the PDMS substrate, as well as inactivated sites where there are only weak van der Waals interactions. Let  $W_{\text{act}}$  and  $W_{\text{in}}$  denote the widths of activated and inactivated sites, respectively [Fig. 15(a)]. Thin ribbons parallel to the prestrain direction are then attached to the prestrained and patterned PDMS substrate [Fig. 15(b)], followed by the relaxation of the prestrained PDMS, which leads to buckling of these ribbons due to the physical separation of the ribbons from the inactivated sites on the PDMS [Fig. 15(c)]. The wavelength of the buckled structures is then given by  $2L_1 = W_{\text{in}} / (1 + \varepsilon_{\text{pre}})$  due to the geometrical constrain, and the amplitude  $A$  depend on the geometries of the interfacial patterns ( $W_{\text{act}}$  and  $W_{\text{in}}$ ) and the prestrain. Figure 15(d) shows a tilted-view scanning electron microscope (SEM) image of buckled GaAs ribbons on PDMS, in which  $\varepsilon_{\text{pre}} = 60\%$ ,  $W_{\text{act}} = 10 \mu\text{m}$ , and  $W_{\text{in}} = 400 \mu\text{m}$ .

Jiang *et al.*<sup>51</sup> developed an analytical model to study the buckling behavior of such systems and to predict the maximum strain in the ribbons as a function of the interfacial pattern. The buckling profile can be expressed as

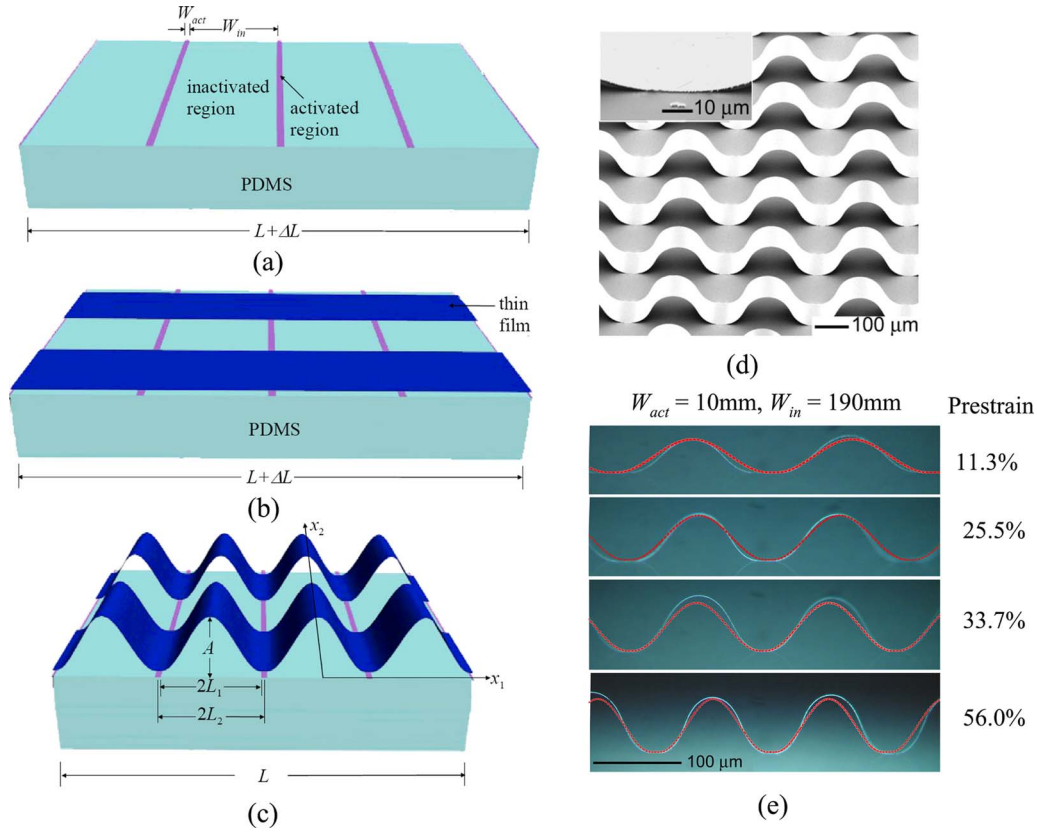


FIG. 15. (Color online) (a) Prestrained PDMS with periodic activated and inactivated patterns. (b) A thin film parallel to the prestrain direction is attached to the prestrained and patterned PDMS substrates. (c) The relaxation of the prestrain  $\varepsilon_{pre}$  in PDMS leads to buckles of thin film. (d) SEM image of buckled GaAs thin films formed using the above procedures (a)–(c). The inset shows the GaAs/PDMS substrate interface. (e) Buckled GaAs thin films on patterned PDMS substrate with  $W_{act}=10 \mu\text{m}$  and  $W_{in}=190 \mu\text{m}$  for different prestrain levels: 11.3%, 25.5%, 33.7%, and 56.0% (from top to bottom). The red lines are the profiles of the buckled GaAs thin film predicted by the analytical solution. (Reprinted with permission from Ref. 51.)

$$w = \begin{cases} w_1 = \frac{1}{2}A \left( 1 + \cos \frac{\pi x_1}{L_1} \right), & -L_1 < x_1 < L_1 \\ w_2 = 0, & L_1 < |x_1| < L_2, \end{cases} \quad (42)$$

where  $A$  is the buckling amplitude to be determined,  $2L_1 = W_{in}/(1 + \varepsilon_{pre})$  is the buckling wavelength, and  $2L_2 = W_{in}/(1 + \varepsilon_{pre}) + W_{act}$  is the sum of activated and inactivated regions after relaxation [Fig. 15(c)].

The energy method was used to determine the buckling amplitude. The bending and membrane energies are

$$U_b = \frac{\pi^4 \bar{E}_f h_f^3 A^2}{96 L_1^3} \quad (43)$$

and

$$U_m = \bar{E}_f h_f \left( \frac{\pi^2 A^2}{16 L_1 L_2} - \varepsilon_{pre} \right)^2 L_2. \quad (44)$$

The relaxed PDMS has vanishing energy

$$U_s = 0 \quad (45)$$

because the substrate has zero displacement at the interface that remains intact  $2(L_2 - L_1)$  as shown in Fig. 15(d) and vanishing stress traction at the long and buckled portion  $2L_1$ .

The buckling amplitude  $A$  is determined by energy minimization as

$$A = \frac{4}{\pi} \sqrt{L_1 L_2 (\varepsilon_{pre} - \varepsilon_c)} \quad \text{for } \varepsilon_{pre} > \varepsilon_c, \quad (46)$$

where  $\varepsilon_c = h_f^2 \pi^2 / 12 L_1^2$  is the critical strain for buckling, which is identical to the Euler buckling strain for a doubly clamped beam with length  $2L_1$ . The critical strain  $\varepsilon_c$  is very small in most practical applications. For example, for the buckling wavelength  $2L_1 \sim 200 \mu\text{m}$  and ribbon thickness  $h_f \sim 0.1 \mu\text{m}$ ,  $\varepsilon_c$  is of the order of  $10^{-6}$ . The buckling amplitude  $A$  in Eq. (46) then can be approximately by

$$A \approx \frac{4}{\pi} \sqrt{L_1 L_2 \varepsilon_{pre}} = \frac{2}{\pi} \sqrt{W_{in} (W_{in} + W_{act}) \varepsilon_{pre} / (1 + \varepsilon_{pre})}, \quad (47)$$

which is completely determined by the interfacial patterns ( $W_{in}$  and  $W_{act}$ ) and the prestrain. Figure 15(e) shows the profiles (red lines) of buckled GaAs ribbons given by Eqs. (42) and (46) for different prestrain levels for  $W_{act}=10 \mu\text{m}$  and  $W_{in}=190 \mu\text{m}$  as well as experimental images. Both wavelength and amplitude agree well with experiments.

Since the membrane strain  $\varepsilon_{11}$  is negligible ( $\sim 10^{-6}$ ), the peak strain in the ribbon is the bending strain which is given by

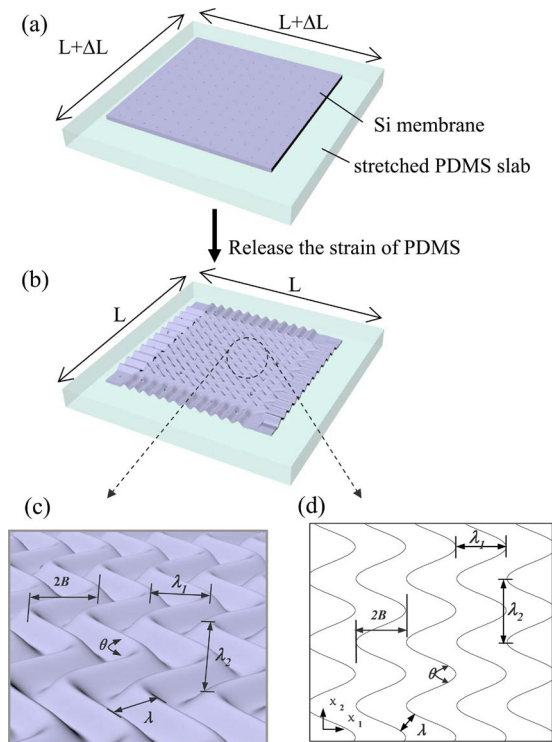


FIG. 16. (Color online) Schematic illustration of the process for fabricating two-dimensional wavy Si nanomembranes on a PDMS substrate. (a) Si membrane is bonded on the stretched PDMS, (b) formation of 2D wavy patterns when PDMS is relaxed, (c) herringbone mode, and (d) top-down view of the herringbone mode. (Reprinted with permission from Ref. 52.)

$$\varepsilon_{\text{peak}} = \frac{h_f}{2} \max \left( \frac{d^2 w}{dx_1^2} \right) = \frac{h_f \pi}{L_1^2} \sqrt{L_1 L_2 \varepsilon_{\text{pre}}}. \quad (48)$$

The peak strain is much smaller than the prestrain. For example,  $\varepsilon_{\text{peak}}$  is only 0.6% for  $h_f = 0.3 \mu\text{m}$ ,  $W_{\text{act}} = 10 \mu\text{m}$ ,  $W_{\text{in}} = 400 \mu\text{m}$ , and  $\varepsilon_{\text{pre}} = 60\%$ . Therefore, the precisely controlled buckling can significantly reduce the maximum strain in thin ribbon and improve the system stretchability. For much smaller active region (i.e.,  $W_{\text{act}} \ll W_{\text{in}}$ ), the peak strain in Eq. (48) can be approximated by  $\varepsilon_{\text{peak}} \approx h_f \pi / L_1 \sqrt{\varepsilon_{\text{pre}}}$ .

It should be pointed out that, for the length of bonded region much larger than the wavelength in Eq. (12), there exists another buckling mode in which the bonded region also buckles. The analysis of this second buckling mode is not presented in this article.

### III. MECHANICS OF STRETCHABLE NANOMEMBRANES

Stretchable nanoribbons can improve the stretchability in the ribbon direction. Most practical applications,<sup>2,5</sup> however, require stretchability in all directions. Choi *et al.*<sup>22</sup> and Song *et al.*<sup>52</sup> produced biaxially stretchable wavy silicon nanomembranes on elastomeric PDMS substrates to provide full 2D stretchability. The fabrication process is illustrated in Fig. 16. The Si nanomembrane is chemically bonded to a heated PDMS substrate which induces a controlled degree of isotropic thermal expansion [Fig. 16(a)]. Cooling to room

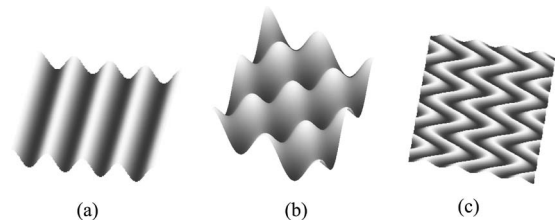


FIG. 17. Schematic illustrations of different buckling modes (a) 1D mode, (b) checkerboard mode from Eq. (51), and (c) herringbone mode from Eq. (59) with  $A = 1.0 \mu\text{m}$ ,  $k_1 = 0.309 \mu\text{m}^{-1}$ ,  $B = 10 \mu\text{m}$ , and  $k_2 = 0.139 \mu\text{m}^{-1}$ . (Reprinted with permission from Ref. 52.)

temperature released the thermally induced prestrain in PDMS and formed the 2D wavy patterns on the surface [Fig. 16(b)]. These patterns exhibited different behaviors at different locations. 1D periodic waves [Fig. 17(a)] predominated near the edges, 2D herringbone layouts [Figs. 16(c), 16(d), and 17(c)] were typically observed at the inner regions, and disordered herringbone structures often occurred near the centers.

The images in Figs. 16 and 17(c) clearly show that the herringbone patterns are characterized by zigzag structures that define two characteristic directions even though the compressive strain is completely isotropic. The herringbone pattern can be characterized by the following parameters, which include the short wavelength  $\lambda$  (the perpendicular distance between adjacent sinusoidal contours), the long wavelength  $\lambda_2 = 2\pi/k_2$  (the distance associated with the separation between adjacent jogs), the amplitude of wave out of plane of the film  $A$ , the jogs wavelength  $\lambda_1 = 2\pi/k_1$ , the amplitude  $B$  of the jogs in the plane of the membrane, and the jog angle  $\theta$ . All above parameters except for the amplitude  $A$  are illustrated in Figs. 16(c) and 16(d), where  $\lambda_1$  and  $\lambda_2$  are along the  $x_1$  and  $x_2$  directions, respectively.

There are extensive numerical studies on the buckling of two-dimensional stiff thin films on compliant substrates. Huang *et al.*<sup>31</sup> developed a spectral method to study the 2D buckling problems. They found that checkerboard mode occurs when the prestrain just exceeds the critical buckling strain and then herringbone mode appears as the prestrain increases. Chen and Hutchinson<sup>53</sup> established a finite element model to obtain the energy for the three buckling modes and showed that the herringbone mode has the lowest energy. They also studied the energy dependence on the geometry of herringbone mode and found that the energy is insensitive to the long wavelength and the jog angle is about  $90^\circ$ . Huang and Im<sup>54</sup> used the spectral method to study two-dimensional wrinkling of a stiff thin film on a viscoelastic substrate. All these studies showed that the herringbone structures are preferred compared to the 1D [Fig. 17(a)] and the checkerboard modes [Fig. 17(b)].

Song *et al.*<sup>52</sup> used the energy method to perform an analytical study of 1D, checkerboard, and herringbone modes (Fig. 17). The analytical study has the advantage over the numerical methods to isolate each buckling mode and calculate its energy. The thin film is modeled as an elastic von Karman plate with finite rotation and the substrate is mod-

eled as a semi-infinite 3D elastic solid. The solutions for 1D, checkerboard, and herringbone modes have been obtained in the following.

*One-dimensional buckling mode.* The out-of-plane displacement of the 1D buckling mode [Fig. 17(a)] is the same as Eq. (1) for the ribbon. The film bending and membrane energy and the substrate energy are obtained analytically as

$$U_b = \frac{\bar{E}_f h_f^3}{48} k_1^4 A^2, \quad (49)$$

$$U_m = \frac{\bar{E}_f h_f}{2} \left[ \left( \frac{1}{4} k_1^2 A^2 - \varepsilon_{11}^{\text{pre}} \right)^2 + (\varepsilon_{22}^{\text{pre}})^2 - 2\nu_f \left( \frac{1}{4} k_1^2 A^2 - \varepsilon_{11}^{\text{pre}} \right) \varepsilon_{22}^{\text{pre}} \right], \quad (50)$$

$$U_s = \frac{\bar{E}_s}{8} k_1 A^2, \quad (51)$$

where  $\varepsilon_{11}^{\text{pre}}$  and  $\varepsilon_{22}^{\text{pre}}$  are the prestrains. Energy minimization gives the same wavelength ( $2\pi/k_1$ ) in Eq. (12) and is independent of the prestrains. For the plane-strain deformation ( $\varepsilon_{22}^{\text{pre}}=0$ ), the amplitude is still given by Eq. (12). For the equibiaxial prestrains  $\varepsilon_{11}^{\text{pre}}=\varepsilon_{22}^{\text{pre}}=\varepsilon_{\text{pre}}$ , the amplitude becomes

$$A = h_f \sqrt{\frac{\varepsilon_{\text{pre}}}{\varepsilon_{1D}^c} - 1}, \quad (52)$$

where  $\varepsilon_{1D}^c = (3\bar{E}_s/\bar{E}_f)^{2/3}/4(1+\nu_f)$  is the critical strain for the 1D buckling mode subjected to equibiaxial prestrains.

*Checkerboard buckling mode.* The out-of-plane displacement of generalized checkerboard mode, as shown in Fig. 17(b), is given by

$$w = A \cos(k_1 x_1) \cos(k_2 x_2). \quad (53)$$

The checkerboard mode is the mode for  $k_1=k_2$ . The film bending and membrane energy and the substrate energy are obtained analytically as

$$U_b = \frac{\bar{E}_f h_f^3}{96} (k_1^2 + k_2^2)^2 A^2, \quad (54)$$

$$U_m = \frac{\bar{E}_f h_f}{256} [A^4 (3 - \nu_f^2) (k_1^4 + k_2^4) + 4\nu_f A^4 k_1^2 k_2^2 - 32A^2 (k_1^2 + \nu_f k_2^2) \varepsilon_{11}^{\text{pre}} - 32A^2 (k_2^2 + \nu_f k_1^2) \varepsilon_{22}^{\text{pre}} + 128(\varepsilon_{11}^{\text{pre}})^2 + 128(\varepsilon_{22}^{\text{pre}})^2 + 256\nu_f \varepsilon_{11}^{\text{pre}} \varepsilon_{22}^{\text{pre}}], \quad (55)$$

$$U_s = \frac{\bar{E}_s}{16} \sqrt{k_1^2 + k_2^2} A^2. \quad (56)$$

For the equibiaxial prestrains  $\varepsilon_{11}^{\text{pre}}=\varepsilon_{22}^{\text{pre}}=\varepsilon_{\text{pre}}$ , the minimization of total energy gives the wave numbers and amplitude as

$$k_1 = k_2 = \frac{1}{\sqrt{2}} \frac{1}{h_f} \left( \frac{3\bar{E}_s}{\bar{E}_f} \right)^{1/3}, \quad (57)$$

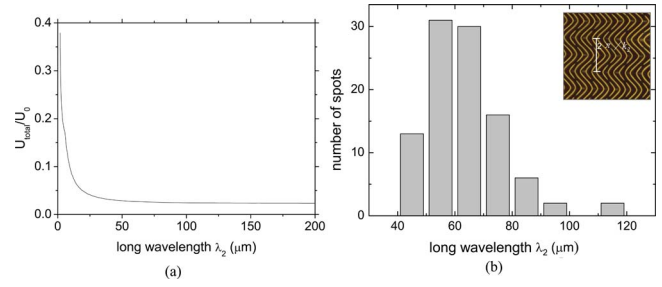


FIG. 18. (Color online) (a) The predicted ratio of total energy in the buckled state to its counterpart in the unbuckled state,  $U_{\text{tot}}/U_0$ , vs the long wavelength  $\lambda_2$  for herringbone mode under 2.4% prestrain. (b) Histogram of long wavelength evaluated at various points in the same sample of the experiment. The film thickness is 100 nm. (Reprinted with permission from Ref. 52.)

$$A = h_f \sqrt{\frac{8}{(3 - \nu_f)(1 + \nu_f)} \left( \frac{\varepsilon_{\text{pre}}}{\varepsilon_{\text{checker board}}^c} - 1 \right)}, \quad (58)$$

where  $\varepsilon_{\text{checker board}}^c = (3\bar{E}_s/\bar{E}_f)^{2/3}/4(1+\nu_f)$  is the critical strain for the checkerboard buckling mode and is the same as that for the 1D buckling mode.

*Herringbone buckling mode.* The out-of-plane displacement  $w$  of the herringbone mode, as shown in Fig. 17(c), can be represented by

$$w = A \cos\{k_1[x_1 + B \cos(k_2 x_2)]\} \quad (59)$$

or

$$w = \sum_{n=0}^{\infty} [A_{1n} \cos(k_1 x_1) \cos(nk_2 x_2) + B_{1n} \sin(k_1 x_1) \cos(nk_2 x_2)], \quad (60)$$

where  $A_{1n}$  and  $B_{1n}$  are the Fourier coefficients of  $A \cos[k_1 B \cos(k_2 x_2)]$  and  $-A \sin[k_1 B \cos(k_2 x_2)]$ , respectively. The bending energy and substrate energy can be obtained analytically as

$$U_b = \frac{\bar{E}_f h_f^3}{384} k_1^2 A^2 (8k_1^2 k_2^2 B^2 + 4k_2^4 B^2 + 3k_1^2 k_2^4 B^4 + 8k_1^2), \quad (61)$$

$$U_s = \frac{\bar{E}_s}{16} \sum_{n=1}^{\infty} \sqrt{k_1^2 + n^2 k_2^2} (A_{1n}^2 + B_{1n}^2) + \frac{\bar{E}_s}{8} k_1 (A_{10}^2 + B_{10}^2). \quad (62)$$

The membrane energy can also be obtained analytically in terms of  $A_{1n}$  and  $B_{1n}$ .<sup>52</sup> The quasi-Newton and finite difference gradient method is used to minimize the total energy and to determine  $A$ ,  $B$ ,  $k_1$ , and  $k_2$ .

Figure 18(a) shows the ratio of total energy  $U_{\text{tot}}$  in the buckled state to that in the unbuckled state  $U_0 = \bar{E}_f h_f (1 + \nu_f) \varepsilon_{\text{pre}}^2$  versus the long wavelength  $\lambda_2$  for the herringbone mode under 2.4% prestrain for 100-nm-thick Si thin film. The curve clearly shows that the total energy is independent of  $\lambda_2$  once  $\lambda_2$  exceeds 110  $\mu\text{m}$ . This long wavelength independent energy has also been observed in the finite element analysis.<sup>53</sup> It also agrees well with the experimental observa-

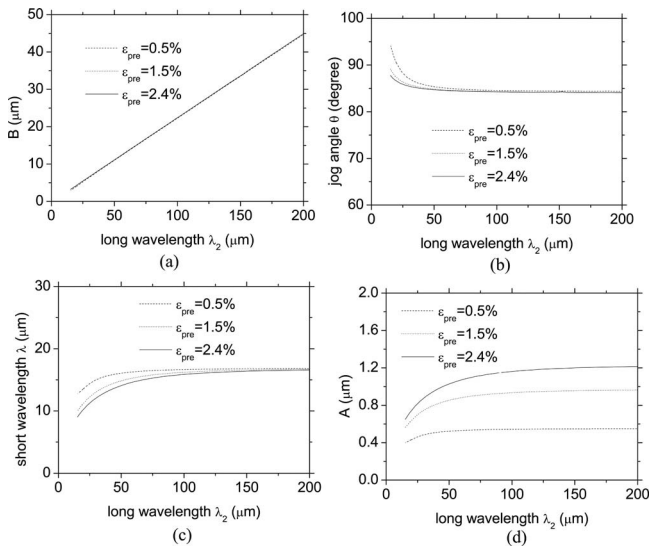


FIG. 19. Predicted (a) amplitude of jogs  $B$ , (b) jog angle  $\theta$ , (c) short wavelength  $\lambda$  and (d) amplitude  $A$  vs long wavelength  $\lambda_2$  for herringbone mode under 0.5%, 1.5%, and 2.4% prestrains. The film thickness is 100 nm. (Reprinted with permission from Ref. 52.)

tions shown in Fig. 18(b), which gives the distribution of long wavelength for 100 points at different places in the same sample.

Figure 19(a) shows the amplitude of jogs  $B$  versus the long wavelength  $\lambda_2$  for three different prestrains, 0.5%, 1.5%, and 2.4%.  $B$  is linearly proportional to  $\lambda_2$  and is independent of the prestrain since there is no difference for all three lines. Figures 19(b) and 19(c) show the jog angle  $\theta$  and short wavelength  $\lambda$ , which are obtained by using  $B \cos(k_2 x_2)$  as the first term of Fourier series of the zigzag function versus the long wavelength, respectively. Except for  $\lambda_2$  less than 20  $\mu\text{m}$ , both the jog angle and short wavelength are essentially independent of the prestrain. The jog angle is close to 90° and the short wavelength is 17  $\mu\text{m}$ . Figure 19(d) shows the amplitude  $A$  versus  $\lambda_2$ . For large  $\lambda_2$ ,  $A$  have a strain-dependent asymptote. The above observations in Fig. 19 also agree with the finite element analysis.<sup>53</sup>

Figure 20(a) shows the ratio of total energy  $U_{\text{tot}}$  in the buckled state to that in the unbuckled state  $U_0$  for three different buckling modes: 1D, checkerboard, and herringbone. The herringbone mode is energetically favorable in 2D buckling since it has the lowest energy. Figures 20(b)–20(d) show the ratios of substrate strain energy  $U_s$ , thin film bending energy  $U_b$ , and membrane energy  $U_m$  to  $U_0$ , which explains why the herringbone mode is often observed in experiments instead of 1D and checkerboard modes. The herringbone mode significantly reduces the thin film membrane energy at the expense of a slight increase in the thin film bending energy and substrate strain energy.

#### IV. MECHANICS OF NONCOPLANAR MESH DESIGN

The analysis in Secs. II and III examined strategies to produce stretchable devices based on wavelike Si nanorib-

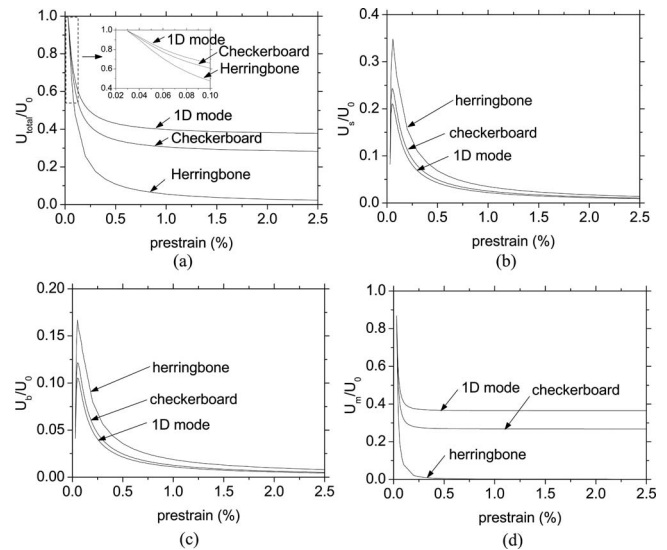


FIG. 20. Predicted ratios of energy in the buckled state to that in the unbuckled state  $U_0$  vs the prestrain  $\epsilon_{\text{pre}}$  for 1D, checkerboard, and herringbone modes. (a) Total energy  $U_{\text{tot}}$  in the Si film/PDMS substrate system, (b) strain energy  $U_s$  in the PDMS substrate, (c) bending energy  $U_b$  in the Si film, and (d) membrane energy  $U_m$  in the Si film. (Reprinted with permission from Ref. 52.)

bons or nanomembranes. Another strategy is to develop interconnect-island mesh designs to increase the stretchability. Such a structure requires interconnects to be stretchable. Lacour *et al.*<sup>25</sup> developed a coplanar mesh design by using stretchable metal electrodes with layouts similar to those of ribbons in Sec. II to interconnect separately fabricated circuit elements. With originally reported procedures, large scale integration might be difficult. Kim *et al.*<sup>26</sup> reported an alternative, in which an entire, ultrathin circuit system is fabricated in a first step, followed by integration with a prestrained substrate to form wavy interconnects upon strain relaxation. Figure 21 shows an optical image of stretchable complementary metal oxide silicon (CMOS) inverters based on this design. Although such layouts can improve the stretchability, it remains too small for certain applications.<sup>2,5</sup> Ko *et al.*<sup>2</sup> and

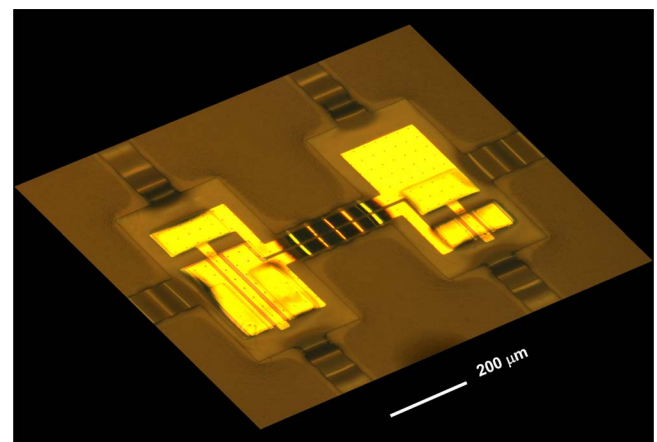


FIG. 21. (Color online) Optical image of CMOS inverters with coplanar mesh design. (Reprinted with permission from Ref. 26.)

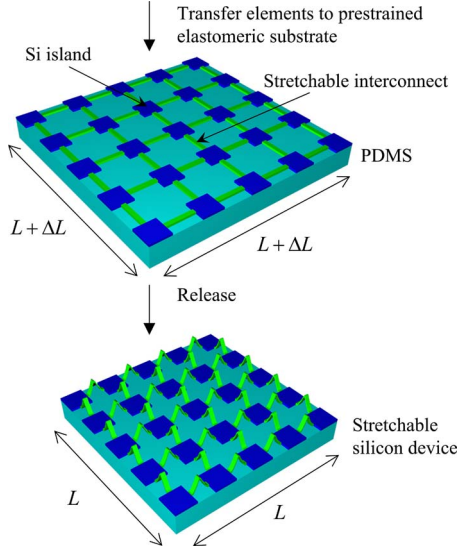


FIG. 22. (Color online) Schematic illustration of the process for fabricating electronics with noncoplanar mesh designs on a compliant substrate. (Reprinted with permission from Ref. 55.)

Kim *et al.*<sup>27</sup> combined the strengths of the precisely controlled buckling in Sec. II E and interconnect-island mesh design to develop a noncoplanar mesh design that avoids these limitations.

Figure 22 schematically illustrates the fabrication of circuits with noncoplanar mesh design on compliant substrates.<sup>2,27</sup> The interconnect-island mesh design is first obtained on a wafer through a patterned layer of photoresist. The mesh design is then lifted off the wafer onto slab of PDMS to deposit a thin layer of Cr/SiO<sub>2</sub> at the locations of Si islands (or other semiconductor materials). Transferring the mesh design to a biaxially stretched PDMS substrate with its surface exposure to ozone forms strong chemical bonds at the locations of the islands and weak bonds at the locations of interconnects. Once the prestrain is released, the interconnects buckle and move out of the plane to accommodate the deformations such that the strain in the islands is very small.

Song *et al.*<sup>55</sup> established a mechanics model to understand the underlying physics and to guide the design of such systems.

### A. Mechanics model of interconnects

The “bridgelike” interconnect is modeled as a beam with clamped ends (as shown in Fig. 23). The out-of-plane displacement  $w$  of the interconnect takes the form

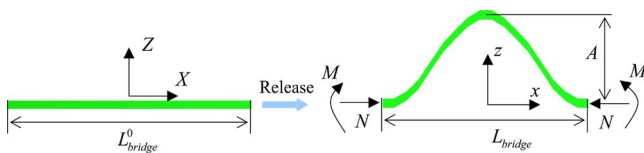


FIG. 23. (Color online) Schematic diagram of mechanics model for the interconnect region of a noncoplanar mesh structure. (Reprinted with permission from Ref. 55.)

$$w = \frac{A}{2} \left( 1 + \cos \frac{2\pi x}{L_{\text{bridge}}} \right) = \frac{A}{2} \left( 1 + \cos \frac{2\pi X}{L_{\text{bridge}}^0} \right) \quad (63)$$

in the strain-free configuration  $X$  of the beam (top figure in Fig. 22) as well as the buckled configuration  $x$  (bottom figure in Fig. 22). Here,  $L_{\text{bridge}}^0$  and  $L_{\text{bridge}}$  are the distances between islands before relaxation and after relaxation, respectively, and the amplitude  $A$  is to be determined by energy minimization.

The bending energy  $U_{\text{bridge}}^{\text{bending}}$  and membrane energy  $U_{\text{bridge}}^{\text{membrane}}$  in the interconnect are obtained as

$$U_{\text{bridge}}^{\text{bending}} = \frac{E_{\text{bridge}} h_{\text{bridge}}^3}{12} \frac{\pi^4 A^2}{(L_{\text{bridge}}^0)^3} \quad (64)$$

and

$$U_{\text{bridge}}^{\text{membrane}} = \frac{1}{2} E_{\text{bridge}} h_{\text{bridge}} L_{\text{bridge}}^0 \left[ \frac{\pi^2 A^2}{4(L_{\text{bridge}}^0)^2} + \frac{L_{\text{bridge}} - L_{\text{bridge}}^0}{L_{\text{bridge}}^0} \right]^2 \quad (65)$$

where  $E_{\text{bridge}}$  is Young's modulus of the interconnect.

Minimization of the total energy (sum of bending and membrane energy) in the interconnect with respect to the amplitude  $A$  gives the amplitude

$$A = \frac{2L_{\text{bridge}}^0}{\pi} \sqrt{\frac{L_{\text{bridge}}^0 - L_{\text{bridge}}}{L_{\text{bridge}}^0} - \varepsilon_c}, \quad (66)$$

where  $\varepsilon_c = \pi^2 h_{\text{bridge}}^2 / [3(L_{\text{bridge}}^0)^2]$  is the critical buckling strain for Euler buckling of a doubly clamped beam. The maximum (compressive) strain in the interconnect is the sum of bending (curvature  $\times h_{\text{bridge}}/2$ ) and membrane strains ( $-\varepsilon_c$ ) and is given by

$$\begin{aligned} \varepsilon_{\text{bridge}}^{\text{max}} &= 2\pi \frac{h_{\text{bridge}}}{L_{\text{bridge}}^0} \sqrt{\frac{L_{\text{bridge}}^0 - L_{\text{bridge}}}{L_{\text{bridge}}^0} - \varepsilon_c} + \varepsilon_c \\ &\approx 2\pi \frac{h_{\text{bridge}}}{L_{\text{bridge}}^0} \sqrt{\frac{L_{\text{bridge}}^0 - L_{\text{bridge}}}{L_{\text{bridge}}^0}}, \end{aligned} \quad (67)$$

where the approximation holds for  $(L_{\text{bridge}}^0 - L_{\text{bridge}})/L_{\text{bridge}}^0 \gg h_{\text{bridge}}^2/(L_{\text{bridge}}^0)^2$ . The prestrain is  $\varepsilon_{\text{pre}} = (L_{\text{bridge}}^0 - L_{\text{bridge}})/L_{\text{bridge}}^0$ . The maximum strain in the interconnect in Eq. (67) then becomes

$$\varepsilon_{\text{bridge}}^{\text{max}} = 2\pi \frac{h_{\text{bridge}}}{L_{\text{bridge}}^0} \sqrt{\frac{\varepsilon_{\text{pre}}}{1 + \varepsilon_{\text{pre}}}}. \quad (68)$$

For the interconnects with  $L_{\text{bridge}}^0 = 20 \mu\text{m}$  and  $h_{\text{bridge}} = 50 \text{ nm}$  in the experiments, the critical buckling strain is  $\varepsilon_c = 0.0021\%$ . For the prestrain  $\varepsilon_{\text{pre}} = 14.3\%$ , which corresponds to  $L_{\text{bridge}} = 17.5 \mu\text{m}$  after relaxation, the analytical prediction of the amplitude from Eq. (66) is  $A = 4.50 \mu\text{m}$ , which agrees well with the experimental value of  $4.76 \mu\text{m}$ . Equation (67) gives the maximum strain in the interconnect as  $0.56\%$ , which is much smaller than the fracture strain of silicon ( $\sim 1\%$ ) and the prestrain  $\varepsilon_{\text{pre}}$ .

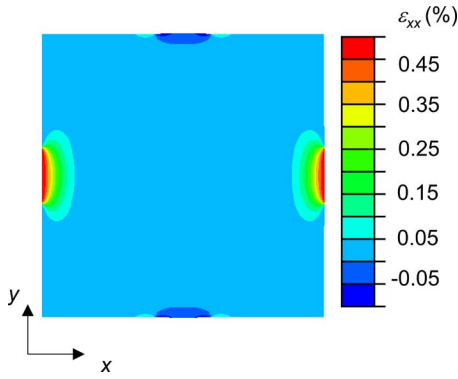


FIG. 24. (Color online) Distribution of the strain  $\varepsilon_{xx}$  in islands ( $20 \times 20 \mu\text{m}^2$ ) when the interconnect relaxes from 20 to 17.5  $\mu\text{m}$ . (Reprinted with permission from Ref. 55.)

As shown in Eq. (67) or Eq. (68), the maximum strain in the interconnect  $\varepsilon_{\text{bridge}}^{\text{max}}$  is proportional to the ratio of the interconnect thickness to the length,  $h_{\text{bridge}}/L_{\text{bridge}}^0$ . Therefore thin and long interconnects give small strain, which provides a design rule for the noncoplanar design to increase the stretchability.

## B. Mechanics model of islands

Circuitry lands, in general, involve multiple layers of different materials,<sup>2,26,27</sup> such as polyimide, metal, Si, and  $\text{SiO}_2$  shown in Fig. 21. Only the Si circuitry is considered in this section, though the analysis can be easily extended to multilayer materials by replacing the corresponding tension and bending rigidities.

The finite element method is used to study the silicon island ( $L_{\text{island}}^0 \times L_{\text{island}}^0$ ) on PDMS substrate [ $(L_{\text{island}}^0 + L_{\text{bridge}}) \times (L_{\text{island}}^0 + L_{\text{bridge}})$ ]. The island is modeled by shell elements and the substrate by 3D solid elements. The island is bonded to the substrate by sharing the same nodes. Periodic conditions are applied on the lateral surfaces ( $X$ - $Z$  and  $Y$ - $Z$  planes). The axial force  $N = E_{\text{bridge}} h_{\text{bridge}} \varepsilon_c$  and bending moment

$$M = \frac{E_{\text{bridge}} h_{\text{bridge}}^3}{12} \frac{2\pi^2 A}{(L_{\text{bridge}}^0)^2} \approx \frac{\pi E_{\text{bridge}} h_{\text{bridge}}^3}{3L_{\text{bridge}}^0} \sqrt{\frac{\varepsilon_{\text{pre}}}{1 + \varepsilon_{\text{pre}}}}$$

from the buckled interconnects are applied over the width  $w_{\text{bridge}}$  on each edge of the island. Since the axial force  $N$  scales with the critical buckling strain  $\varepsilon_c$  ( $\sim 10^{-5}$ ), the strain due to the axial force  $N$  is negligible compared to the strain due to the bending moment  $M$  (i.e., bending dominates).

For the noncoplanar mesh design with interconnect ( $E_{\text{bridge}} = 130 \text{ GPa}$ ,  $\nu_{\text{bridge}} = 0.27$ ,  $L_{\text{bridge}}^0 = 20 \mu\text{m}$ ,  $h_{\text{bridge}} = 50 \text{ nm}$ ,  $w_{\text{bridge}} = 4 \mu\text{m}$ , and  $L_{\text{bridge}} = 17.5 \mu\text{m}$  after relaxation) and island ( $E_{\text{island}} = 130 \text{ GPa}$ ,  $\nu_{\text{island}} = 0.27$ , length  $L_{\text{island}}^0 = 20 \mu\text{m}$ , and thickness  $h_{\text{island}} = 50 \text{ nm}$ ), Fig. 24 shows the finite element result of strain distribution  $\varepsilon_{xx}$  in a Si island. The maximum strain occurs at the interconnect/island boundary. Since the strain due to the axial force is negligible

as compared to the bending moment, the dimensional analysis and finite element analysis give the maximum strain in the silicon island as<sup>55</sup>

$$\begin{aligned} \varepsilon_{\text{island}}^{\text{max}} &\approx \frac{6(1 - \nu_{\text{island}}^2)M}{E_{\text{island}} h_{\text{island}}^2} \\ &= 2\pi \frac{(1 - \nu_{\text{island}}^2)E_{\text{bridge}} h_{\text{bridge}}^3}{E_{\text{island}} h_{\text{island}}^2 L_{\text{bridge}}^0} \sqrt{\frac{\varepsilon_{\text{pre}}}{1 + \varepsilon_{\text{pre}}}}, \end{aligned} \quad (69)$$

which clearly shows that stiff and thick island reduces its strain.

The maximum allowable prestrain  $\varepsilon_{\text{pre}}^{\text{max}}$  that the noncoplanar mesh design can accommodate is obtained by  $\varepsilon_{\text{bridge}}^{\text{max}} = \varepsilon_{\text{bridge}}^{\text{failure}}$  and  $\varepsilon_{\text{island}}^{\text{max}} = \varepsilon_{\text{island}}^{\text{failure}}$  as

$$\varepsilon_{\text{pre}}^{\text{max}} < \frac{a^2}{1 - a^2} \quad \text{if } a < 1, \quad (70)$$

where

$$a = \frac{L_{\text{bridge}}^0}{2\pi h_{\text{bridge}}} \min \left[ \varepsilon_{\text{bridge}}^{\text{failure}} \frac{E_{\text{island}} h_{\text{island}}^2}{(1 - \nu_{\text{island}}^2) E_{\text{bridge}} h_{\text{bridge}}^2} \varepsilon_{\text{island}}^{\text{failure}} \right]. \quad (71)$$

For  $a < 1$  (e.g., short interconnects), the maximum strain is determined by the failure of interconnect or island, while for  $a \geq 1$  (e.g., long interconnects), the maximum prestrain is governed by the failure of PDMS substrate.

## C. Stretchability/compressibility of noncoplanar mesh design

A unit cell with length  $L_{\text{bridge}}^0 + L_{\text{island}}^0$  before relaxation is considered to obtain the stretchability/compressibility. After relaxation, the interconnect length changes from  $L_{\text{bridge}}^0$  to  $L_{\text{bridge}} = L_{\text{bridge}}^0 / (1 + \varepsilon_{\text{pre}})$ , while the island length remains same because the interconnect buckles to accommodate the release of prestrain. The length of the unit cell then becomes  $L_{\text{bridge}} + L_{\text{island}}^0$ . Once  $\varepsilon_{\text{applied}}$  is applied to the buckled system, the interconnect length changes to  $L'_{\text{bridge}}$  and the length of the unit cell becomes  $L'_{\text{bridge}} + L_{\text{island}}^0$ . The applied strain  $\varepsilon_{\text{applied}}$  is given by

$$\varepsilon_{\text{applied}} = \frac{L'_{\text{bridge}} - L_{\text{bridge}}}{L_{\text{bridge}} + L_{\text{island}}^0}. \quad (72)$$

The stretchability, which characterizes how much the noncoplanar mesh design can accommodate further stretch, is determined by the condition at which the buckled interconnect returns to a flat state (i.e.,  $L'_{\text{bridge}} = L_{\text{bridge}}^0$ ). This condition gives the stretchability as

$$\varepsilon_{\text{stretchability}} = \frac{L_{\text{bridge}}^0 - L_{\text{bridge}}}{L_{\text{bridge}} + L_{\text{island}}^0} = \frac{\varepsilon_{\text{pre}}}{1 + (1 + \varepsilon_{\text{pre}}) \frac{L_{\text{island}}^0}{L_{\text{bridge}}^0}}, \quad (73)$$

which clearly shows that long interconnects, short islands, and large prestrains increase the stretchability. The stretchability is  $\varepsilon_{\text{pre}}$  and

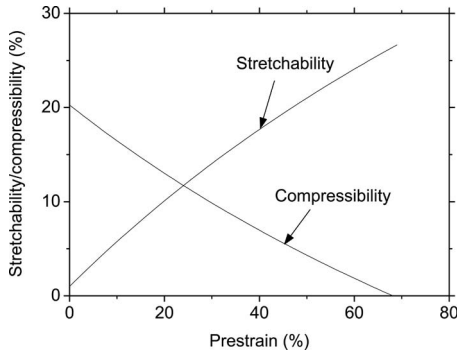


FIG. 25. Predicted stretchability from Eq. (73) and compressibility from Eq. (74) versus the prestrain for the noncoplanar mesh design (island:  $20 \times 20 \mu\text{m}^2$ , 50 nm thick; interconnect:  $20 \times 4 \mu\text{m}^2$ , 50 nm thick) when the failure strains of interconnect and island are 1%. (Reprinted with permission from Ref. 55.)

$$\frac{L_{\text{bridge}}^0 \varepsilon_{\text{pre}}}{L_{\text{island}}^0 (1 + \varepsilon_{\text{pre}})}$$

for the two limit cases of long interconnect  $L_{\text{bridge}}^0 \gg L_{\text{island}}^0$  and short interconnect  $L_{\text{bridge}}^0 \ll L_{\text{island}}^0$ , respectively.

The compressibility, which characterizes how much the noncoplanar mesh design can accommodate further compression, is determined by equating the maximum strains in interconnect and island to corresponding failure strains  $\varepsilon_{\text{bridge}}^{\text{failure}}$  and  $\varepsilon_{\text{island}}^{\text{failure}}$  or the contacting of the neighbor islands. This gives the compressibility as

$$\varepsilon_{\text{compressibility}} = \min \left[ \frac{(1 + \varepsilon_{\text{pre}})a^2 - \varepsilon_{\text{pre}}}{1 + (1 + \varepsilon_{\text{pre}}) \frac{L_{\text{island}}^0}{L_{\text{bridge}}^0}}, \frac{1}{1 + (1 + \varepsilon_{\text{pre}}) \frac{L_{\text{island}}^0}{L_{\text{bridge}}^0}} \right], \quad (74)$$

where  $a$  is given in Eq. (71). The compressibility becomes

$$\frac{1}{1 + (1 + \varepsilon_{\text{pre}}) \frac{L_{\text{island}}^0}{L_{\text{bridge}}^0}}$$

and

$$\frac{(1 + \varepsilon_{\text{pre}})a^2 - \varepsilon_{\text{pre}}}{1 + (1 + \varepsilon_{\text{pre}}) \frac{L_{\text{island}}^0}{L_{\text{bridge}}^0}}$$

for long interconnects (large  $a$ , corresponding to the contact of neighbor islands) and short interconnects (small  $a$ , corresponding to the failure of interconnect or island), respectively.

Figure 25 shows the stretchability and compressibility versus the prestrain for  $L_{\text{island}}^0 = 20 \mu\text{m}$ ,  $h_{\text{island}} = 50 \text{ nm}$ ,  $L_{\text{bridge}}^0 = 20 \mu\text{m}$ ,  $h_{\text{bridge}} = 50 \text{ nm}$ , and  $w_{\text{bridge}} = 4 \mu\text{m}$ . For simplicity, we assume  $\varepsilon_{\text{bridge}}^{\text{failure}} = \varepsilon_{\text{island}}^{\text{failure}} = 1\%$ . As the prestrain increases, the stretchability improves but the compressibility worsens. Therefore, prestrain cannot be used to achieve both maximum stretchability and maximum compressibility. Figure 26 shows the stretchability and compressibility versus

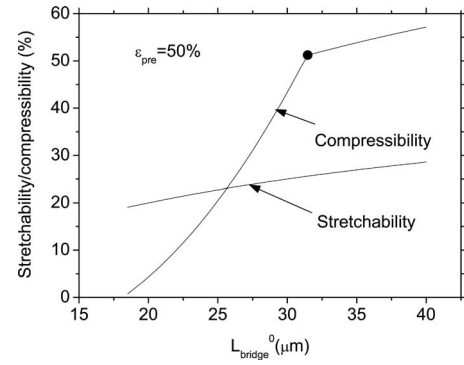


FIG. 26. Predicted stretchability from Eq. (73) and compressibility from Eq. (74) vs the length of interconnect for the noncoplanar mesh design when the prestrain is 50%. The dot on the curve for compressibility separates the failure of interconnect or island (left of the dot) from the contact of neighbor islands (right of the dot). (Reprinted with permission from Ref. 55.)

the interconnect length for the same set of properties as Fig. 25 and the prestrain  $\varepsilon_{\text{pre}} = 50\%$ . As the length of the interconnect increases, both stretchability and compressibility improve. The dot on the curve for compressibility separates the failure of interconnect or island (left of the dot) from the contact of neighbor islands (right of the dot). Therefore, the increase in interconnect length gives both large stretchability and compressibility.

The interconnects described above are straight. To expand the deformability even further, serpentine interconnects can be used.<sup>27</sup> Figure 27 shows a SEM image of such a design after executing the fabrication procedures of Fig. 22. The serpentine interconnects have two major advantages over straight ones: (1) they are much longer than straight interconnects, and therefore can accommodate much larger prestrain; (2) once the applied strain reaches the prestrain, straight interconnects become flat and lose their stretchability, but serpentine interconnects can be stretched much further because large twist will be involved to accommodate larger deforma-

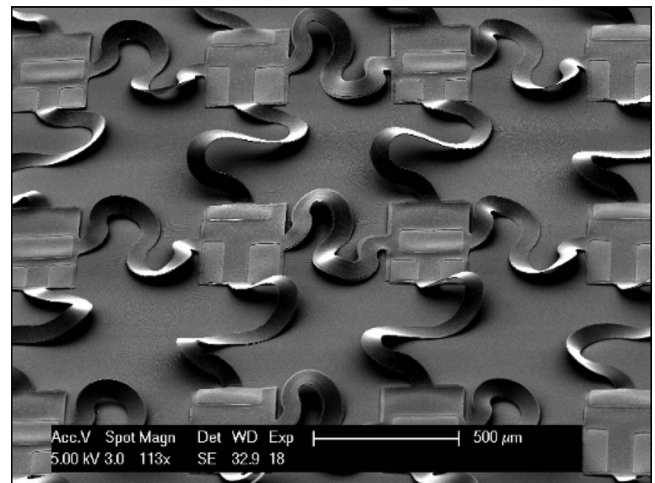


FIG. 27. SEM image of an array of CMOS inverters with noncoplanar mesh design that has serpentine interconnects.

tion. Exploring the noncoplanar mesh design with serpentine interconnects represents a fruitful topic for future work.

## V. CONCLUSION

We have reviewed the mechanics of stretchable inorganic material for stretchable electronics.

*Stretchable nanoribbons.* Both analytical solutions and numerical results show strain-dependent buckling wavelength for stretchable nanoribbons, which agree well with the experiments without any parameter fitting. The strains are accommodated through changes in the amplitudes and wavelengths of buckled geometries. Once the ribbon buckles, its membrane strain remains a constant (the critical strain for buckling), and the peak strain (due to bending) increases very slowly with the applied strain. The critical condition for local and global buckling of thin films on compliant substrates is obtained analytically, and the results agree well with the experimental and numerical studies. The effect of free edges near the ends of the ribbons is studied numerically and found that the unbuckled regions in these areas result from the traction-free boundary conditions. The length of this edge effect is proportional to the film thickness and decreases with increasing prestrain and substrate modulus. The finite width and spacing effects have been studied analytically. The analytical solution is obtained for the ribbon of finite width and spacing. The experimental and analytical results show that both the buckling amplitude and wavelength increase with the film width. Finally, precisely controlled buckling of thin ribbons provides a simple method to significantly increase the system stretchability/compressibility.

*Stretchable nanomembranes.* An analytical model has been established to study the 1D, checkerboard, and herringbone buckling patterns in a stiff thin membrane on a compliant substrate system. The herringbone mode has the lowest energy as compared to the 1D or checkerboard modes because the herringbone mode significantly reduces the membrane energy at the expense of a slight increase in the bending energy and substrate energy.

*Noncoplanar mesh designs.* A mechanics model has been established for stretchable electronics with noncoplanar mesh design. The predicted buckling amplitude agrees well with experiments without any parameter fitting. The maximum strains in the interconnect and island are also obtained analytically and are used to predict the stretchability and compressibility.

## ACKNOWLEDGMENTS

The authors thank T. Banks for various helps in processing by use of facilities at Frederick Seitz Materials Research Laboratory. This material is based on work supported by the National Science Foundation under Grant No. ECCS-0824129, NSFC, and the U.S. Department of Energy, Division of Materials Sciences under Award No. DE-FG02-07ER46471 through the Materials Research Laboratory and Center for Microanalysis of Materials (Grant No. DE-FG02-07ER46453) at the University of Illinois at Urbana-

Champaign. One of the authors (J.S.) acknowledges the financial support from the College of Engineering at the University of Miami.

- <sup>1</sup>G. P. Crawford, *Flexible Flat Panel Display Technology* (Wiley, New York, 2005).
- <sup>2</sup>H. C. Ko *et al.*, *Nature* (London) **454**, 748 (2008).
- <sup>3</sup>H. C. Jin, J. R. Albelson, M. K. Erhardt, and R. G. Nuzzo, *J. Vac. Sci. Technol. B* **22**, 2548 (2004).
- <sup>4</sup>V. J. Lumelsky, M. S. Shur, and S. Wagner, *IEEE Sens. J.* **1**, 41 (2001).
- <sup>5</sup>T. Someya, T. Sekitani, S. Iba, Y. Kato, H. Kawaguchi, and T. Sakurai, *Proc. Natl. Acad. Sci. U.S.A.* **101**, 9966 (2004).
- <sup>6</sup>A. Nathan *et al.*, *Microelectron. J.* **31**, 883 (2000).
- <sup>7</sup>F. Garnier, R. Hajlaoui, A. Yassar, and P. Srivastava, *Science* **265**, 1684 (1994).
- <sup>8</sup>F. Garnier, *Chem. Phys.* **227**, 253 (1998).
- <sup>9</sup>M. A. Baldo, M. E. Thompson, and S. R. Forrest, *Nature* (London) **403**, 750 (2000).
- <sup>10</sup>B. Crone *et al.*, *Nature* (London) **403**, 521 (2000).
- <sup>11</sup>Y. L. Loo, T. Someya, K. W. Baldwin, Z. N. Bao, P. Ho, A. Dodabalapur, H. E. Katz, and J. A. Rogers, *Proc. Natl. Acad. Sci. U.S.A.* **99**, 10252 (2002).
- <sup>12</sup>J. L. Bredas, J. P. Calbert, D. A. da Silva Fiho, and J. Cornil, *Proc. Natl. Acad. Sci. U.S.A.* **99**, 5804 (2002).
- <sup>13</sup>T. W. Kelley, P. F. Baude, C. Gerlach, D. E. Ender, D. Muyres, M. A. Haase, D. E. Vogel, and S. D. Theiss, *Chem. Mater.* **16**, 4413 (2004).
- <sup>14</sup>A. Facchetti, M. H. Yoon, and T. J. Marks, *Adv. Mater. (Weinheim, Ger.)* **17**, 1705 (2005).
- <sup>15</sup>F. C. Chen, C. S. Chuang, Y. S. Lin, L. J. Kung, T. H. Chen, and H. P. D. Shieh, *Org. Electron.* **7**, 435 (2006).
- <sup>16</sup>T. Sekitani, Y. Noguchi, K. Hata, T. Fukushima, T. Aida, and T. Someya, *Science* **321**, 1468 (2008).
- <sup>17</sup>N. Bowden, S. Brittain, A. G. Evans, J. W. Hutchinson, and G. M. Whitesides, *Nature* (London) **393**, 146 (1998).
- <sup>18</sup>T. Ohzono, S. I. Matsushita, and M. Shimomura, *Soft Matter* **1**, 227 (2005).
- <sup>19</sup>K. Efimenko, M. Rackaitis, E. Manias, A. Vaziri, L. Mahadevan, and J. Genzer, *Nature Mater.* **4**, 293 (2005).
- <sup>20</sup>A. Hozumi, T. Masuda, H. Sugimura, and T. Kameyama, *Langmuir* **19**, 7573 (2003).
- <sup>21</sup>D. Y. Khang, H. Jiang, Y. Huang, and J. A. Rogers, *Science* **311**, 208 (2006).
- <sup>22</sup>W. M. Choi, J. Song, D. Y. Khang, H. Jiang, Y. Huang, and J. A. Rogers, *Nano Lett.* **7**, 1655 (2007).
- <sup>23</sup>D. H. Kim *et al.*, *Science* **320**, 507 (2008).
- <sup>24</sup>D. S. Gray, J. Tien, and C. S. Chen, *Adv. Mater. (Weinheim, Ger.)* **16**, 393 (2004).
- <sup>25</sup>S. P. Lacour, J. Jones, S. Wagner, T. Li, and Z. Suo, *Proc. IEEE* **93**, 1459 (2005).
- <sup>26</sup>D. H. Kim *et al.*, *Appl. Phys. Lett.* **93**, 044102 (2008).
- <sup>27</sup>D. H. Kim *et al.*, *Proc. Natl. Acad. Sci. U.S.A.* **105**, 18675 (2008).
- <sup>28</sup>S. Sosin, T. Zoumpoulidis, M. Bartek, L. Wang, R. Dekker, K. M. B. Jansen, and L. J. Ernst, *Proceedings of Electronic Components and Technology Conference, 2008* (unpublished), pp. 1339–1345.
- <sup>29</sup>INSPEC, *Properties of Silicon* (Institution of Electrical Engineers, New York, 1988).
- <sup>30</sup>E. A. Wilder, S. Guo, S. Lin-Gibson, M. J. Fasolka, and C. M. Stafford, *Macromolecules* **39**, 4138 (2006).
- <sup>31</sup>Z. Y. Huang, W. Hong, and Z. Suo, *J. Mech. Phys. Solids* **53**, 2101 (2005).
- <sup>32</sup>C. M. Stafford *et al.*, *Nature Mater.* **3**, 545 (2004).
- <sup>33</sup>C. M. Stafford, B. D. Vogt, C. Harrison, D. Julthongpipit, and R. Huang, *Macromolecules* **39**, 5095 (2006).
- <sup>34</sup>N. Bowden, W. T. S. Huck, K. E. Paul, and G. M. Whitesides, *Appl. Phys. Lett.* **75**, 2557 (1999).
- <sup>35</sup>W. T. S. Huck, N. Bowden, P. Onck, T. Pardoan, J. W. Hutchinson, and G. M. Whitesides, *Langmuir* **16**, 3497 (2000).
- <sup>36</sup>J. S. Sharp and R. A. L. Jones, *Adv. Mater. (Weinheim, Ger.)* **14**, 799 (2002).
- <sup>37</sup>P. J. Yoo, K. Y. Suh, S. Y. Park, and H. H. Lee, *Adv. Mater. (Weinheim, Ger.)* **14**, 1383 (2002).

- <sup>38</sup>H. Schmid, H. Wolf, R. Allenspach, H. Riel, S. Karg, B. Michel, and E. Delamarche, *Adv. Funct. Mater.* **13**, 145 (2003).
- <sup>39</sup>M. W. Moon, S. H. Lee, J. Y. Sun, K. H. Oh, A. Vaziri, and J. W. Hutchinson, *Proc. Natl. Acad. Sci. U.S.A.* **104**, 1130 (2007).
- <sup>40</sup>H. Jiang, D. Y. Khang, J. Song, Y. Sun, Y. Huang, and J. A. Rogers, *Proc. Natl. Acad. Sci. U.S.A.* **104**, 15607 (2007).
- <sup>41</sup>C. Harrison, C. M. Stafford, W. H. Zhang, and A. Karim, *Appl. Phys. Lett.* **85**, 4016 (2004).
- <sup>42</sup>A. L. Volynskii, S. Bazhenov, O. V. Lebedeva, and N. F. Bakeev, *J. Mater. Sci.* **35**, 547 (2000).
- <sup>43</sup>J. Song, H. Jiang, Z. J. Liu, D. Y. Khang, Y. Huang, J. A. Rogers, C. Lu, and C. G. Koh, *Int. J. Solids Struct.* **45**, 3107 (2008).
- <sup>44</sup>K. Symon, *Mechanics* (Addison-Wesley, Reading, MA, 1971).
- <sup>45</sup>S. Wang, J. Song, D. H. Kim, Y. Huang, and J. A. Rogers, *Appl. Phys. Lett.* **93**, 023126 (2008).
- <sup>46</sup>Z. P. Bazant and L. Cedolin, *Stability of Structures* (Dove, New York, 2003).
- <sup>47</sup>C. T. Koh, Z. J. Liu, D. Y. Khang, J. Song, C. Lu, Y. Huang, J. A. Rogers, and C. G. Koh, *Appl. Phys. Lett.* **91**, 133113 (2007).
- <sup>48</sup>H. Jiang, D. Y. Khang, H. Fei, H. Kim, Y. Huang, J. Xiao, and J. A. Rogers, *J. Mech. Phys. Solids* **56**, 2585 (2008).
- <sup>49</sup>M. Abramowitz and I. A. Stegun, *Handbook of Mathematical Functions with Formulas, Graphs, and Mathematical Tables* (Dover, New York, 1972).
- <sup>50</sup>Y. Sun, W. M. Choi, H. Jiang, Y. Huang, and J. A. Rogers, *Nat. Nanotechnol.* **1**, 201 (2006).
- <sup>51</sup>H. Jiang, Y. Sun, J. A. Rogers, and Y. Huang, *Appl. Phys. Lett.* **90**, 133119 (2007).
- <sup>52</sup>J. Song, H. Jiang, W. M. Choi, D. Y. Khang, Y. Huang, and J. A. Rogers, *J. Appl. Phys.* **103**, 014303 (2008).
- <sup>53</sup>X. Chen and J. W. Hutchinson, *ASME Trans. J. Appl. Mech.* **71**, 597 (2004).
- <sup>54</sup>R. Huang and S. H. Im, *Phys. Rev. E* **74**, 026214 (2006).
- <sup>55</sup>J. Song, Y. Huang, J. Xiao, S. Wang, K. C. Hwang, H. C. Ko, D. H. Kim, M. P. Stoykovich, and J. A. Rogers, *J. Appl. Phys.* **105**, 123516 (2009).